Evaluating debris-flow and anthropogenic disturbance on 10Be concentration in mountain drainage basins: implications for functional connectivity and denudation rates across time scales

Evaluating debris-flow and anthropogenic disturbance on ^{10}Be concentration in mountain drainage basins: implications for functional connectivity and denudation rates across time scales

Francesco Brardinoni[1] *, Reto Grischott[2], Florian Kober[2], Corrado Morelli[3], Marcus Christl[4]

1. Department of Biological, Geological and Environmental Sciences, University of Bologna, Bologna, Italy

2. Institute of Geology, ETH Zürich, Zürich, Switzerland

3. Provincia Autonoma di Bolzano, Ufficio Geologia e Prove Materiali, Cardano, Italy

4. Laboratory of Ion Beam Physics, ETH Zürich, Zürich, Switzerland

* Correspondence to: francesco.brardinoni@unibo.it

Manuscript accepted for publication in

Earth Surface Processes and Landforms

24 September 2020

Abstract

We examine the sensitivity of ^{10}Be concentrations (and derived denudation rates), to debris-flow and anthropogenic perturbations in steep settings of the Eastern Alps, and explore possible relations with structural geomorphic connectivity. Using cosmogenic ^{10}Be as a tracer for functional geomorphic connectivity, we conduct sampling replications across four seasons in Gadria, Strimm and Allitz Creek. Sampling sites encompass a range of structural connectivity configurations, including the conditioning of a sackung, all assessed through a geomorphometric index (IC). By combining information on contemporary depth of erosion and sediment yield, disturbance history, and post-LGM sedimentation rates, we constrain the effects of debris-flow disturbance on ^{10}Be concentrations at the Gadria sites. Here, we argue that bedrock weakening imparted by the sackung promotes high depth of erosion. Consequently, debris flows recruit sediment beyond the critical depth of spallogenic production (e.g., > 3 m), which in turn, episodically, due to predominantly muogenic production pathways, lowers ^{10}Be concentration by a factor of 4, for at least 2 years. In contrast, steady erosion in Strimm Creek, yields very stable ^{10}Be concentrations through time. In Allitz Creek, we observe 2- to 4-fold seasonal fluctuations in ^{10}Be concentrations, which we explain as the combined effects of water diversion and hydraulic structures on sediment mixing. We further show that ^{10}Be concentration correlates inversely with the IC index, where sub-basins characterized by high concentrations (long residence times) exhibit low IC values (structurally disconnected) and vice versa, implying that, over millennial time scales a direct relation exists between functional and structural connectivity, and that the IC index performed as a suitable metric for structural connectivity. The index performs comparably better than other metrics (i.e., mean slope and mean normalised channel

steepness index) previously used to assess topographic controls on denudation rates in active unglaciated ranges. In terms of landscape evolution, we argue that the sackung, by favouring intense debris-flow activity across the Holocene, has aided rapid postglacial reshaping of the Gadria basin, which currently exhibits a topographic signature characteristic of unglaciated debris-flow systems.

Keywords: ^{10}Be concentration; denudation rate; debris flow; depth of erosion; geomorphic connectivity; Deep-Seated Gravitational Slope Deformation.

1. Introduction

The relation linking sediment flux to topography forms the functional basis of geomorphology and is critical for understanding landscape evolution, as well as for assessing disturbance and geo-hazard potential (Thorn and Rhoads, 1996). In this context, conceptual and methodological advances in in-situ produced terrestrial cosmogenic nuclides (TCN, e.g., ^{10}Be, ^{14}C and ^{26}Al) carried in alluvial sediment have been critical for inferring average, millennial (10^2-10^4 years), catchment-wide denudation rates (CWDRs) (Brown *et al.,* 1995; Bierman and Steig, 1996; Granger *et al.,* 1996), hence average sediment fluxes (Kirchner *et al.,* 2001). These estimates have allowed bridging the gap between decadal sediment fluxes, derived from river load monitoring (e.g., Church and Slaymaker, 1989; Milliman and Farnsworth, 2011) and/or multi-temporal landslide inventories (e.g., Dadson *et al.,* 2004; Brardinoni *et al.,* 2009), and exhumation rates inferred from low temperature thermochronometry (10^6 years) (e.g., Reiners and Brandon, 2006).

Reliable TCN-derived denudation rates can be obtained in geomorphic systems that fulfill specific working assumptions: (i) the pace of geomorphic processes active in the study basin must be steady in order to obtain steady and constant (over the observed timescale) TCN concentrations under ambient denudation; and (ii) each sub-basin must convey quartz to the outlet in proportion to its average denudation rate as to yield a well-mixed alluvium (Binnie *et al.,* 2006; Neilson *et al.,* 2017). These conditions are considered reasonably well met when each component (e.g., a hillslope and/or a sub-basin) of the fluvial system being sampled exports sediment in proportion to its areal extent and long-term denudation rate (Granger *et al.,* 1996; Binnie *et al.,* 2006; von Blanckenburg, 2006).

Significant departure from appropriate sediment mixing (i.e., well-mixed alluvium) may stem from a number of perturbations, whose effects on average TCN-based CWDRs are still matter of debate (Granger *et al.,* 2013). In mountain drainage basins, potential short- to long-term perturbations can arise from natural and anthropogenic sources, including the transit of sedimentary waves induced by land use changes (Vanacker *et al.,* 2007), or by large catastrophic landslides that can elevate sediment yield for days to millennia (Korup, 2012). Similarly, engineering structures for geo-hazard reduction, or river regulation, reduce sediment export to lowland fluvial systems (Hinderer *et al.,* 2013; Stutenbecker *et al*., 2018), and modify the seasonal to decadal variability of sediment delivery to streams, in-channel sediment storage, as well as the magnitude and frequency of sediment transporting flows (Church, 1995; Grant, 2012). These changes, when altering in-channel sediment mixing, could introduce a bias in ^{10}Be concentrations (hereafter termed [10Be]) and the derived CWDRs, yielding “apparent” denudation rates (Lal, 1991).

Given potential perturbations, there has been concern about whether appropriate mixing will remain consistent at a given study site (e.g., the outlet of a basin) if one repeats sampling at the same location, in a different season, or year (Niemi *et al,* 2005; Binnie *et al.,* 2006; Yanites *et al.* 2009). This concern, which has recently been addressed in steep alpine settings by a handful of studies (Kober *et al.,* 2012; 2019; Delunel *et al.,* 2013, Foster and Anderson, 2016), is conceptually related to the pathways, the travel times and residence times of sediment that cascades across the geomorphic units (e.g., sediment reservoirs) of a given study basin. Put differently, TCN concentration (and the corresponding CWDR) at a sampling location might be related to the degree of geomorphic connectivity in the relevant source basin, where geomorphic connectivity is the propensity of a geomorphic system to favour the

transfer of sediment, through structural (forms and materials) and functional (sediment fluxes) linkages among its building blocks (Heckmann *et al.,* 2018).

The conceptual framework of geomorphic connectivity integrates the *lateral* and *longitudinal* components (Fryirs *et al.,* 2007). The former expresses the degree of proximity between hillslopes and channels, which dictates the capability of hillslope-to-channel sediment delivery, originally defined as *slope-channel geomorphic coupling* (Brunsden and Thornes, 1979; Caine and Swanson, 1982). The latter considers the potential of in-channel downstream sediment conveyance.

Evaluation of structural connectivity – the spatial arrangement of geomorphic units, for example, hillslopes and channels – is typically performed by applying morphometric (IC) indices of connectivity (e.g., Borselli *et al.*, 2008; Cavalli *et al.,* 2013) (Figure 1). The degree of functional connectivity – the spatial and temporal variability of sediment fluxes from sources to (temporary or permanent) sinks – can be assessed via sediment tracing (e.g., Bracken *et al.,* 2015).

Within the wealth of recent empirically-based studies, the relation linking structural to functional connectivity has largely remained elusive (e.g., Alfonso-Torreno *et al.*, 2019). Available information, chiefly deriving from soil erosion and land degradation research, point to a direct, highly scattered relation between sediment flux, inferred from sequential DoD (DEM of Difference), sediment deposition at check-dams, or tracer dispersal, and IC index at the seasonal (Lu *et al.*, 2019), decadal (Sougnez *et al.*, 2011) and the storm event (Chartin *et al.*, 2017) scale. In this context, the nature and the characteristic time scales at which a possible relation between TCN-derived CWDR (sediment flux) and structural geomorphic connectivity (landscape morphometry) may hold, have remained unexplored.

141 This paper aims to address the sensitivity of [10Be] (and derived CWDRs) to short-
142 term (i.e., seasonal to inter-annual) perturbations in steep alpine basins and explore
143 possible interrelations with structural geomorphic connectivity. To pursue these
144 objectives, we repeat ^{10}Be sampling over 3 years in the Gadria (6.3 km^2) and Strimm
145 (8.5 km^2) basins, two adjacent headwater systems that join in Allitz Creek, a man-
146 maintained channel that crosses the anomalously large Gadria fan (10.9 km^2) before
147 entering the Adige River (Figure 2). The two systems were selected as they
148 encompass a wide range of geomorphic conditions, over a small area. They display:
149 (i) high variability in rock strength, due to the presence of a sackung in Gadria
150 (DSGSD in Figure 3) that locally imparts substantial rock weakening (Perina, 2012);
151 (ii) contrasting topographic structure i.e., a simple concave-up long profile in Gadria,
152 as opposed to a complex stepped profile in Strimm (Figure 4); (iii) contrasting spatial
153 patterns of structural geomorphic connectivity (Cavalli *et al.,* 2013); and (iv)
154 contrasting contemporary rates of sediment transfer (Brardinoni *et al.,* 2012; Comiti *et*
155 *al.,* 2014; Dell'Agnese *et al.,* 2015; Cavalli *et al.,* 2017).

156 Using cosmogenic ^{10}Be as a tracer for functional connectivity, we adopt a sampling
157 strategy to track the temporal variability of [10Be] at locations that encompass a
158 range of lateral (hillslope-channel) and longitudinal (within-channel) degrees of
159 structural geomorphic connectivity, evaluated through an IC index. 10Be
160 concentrations, by providing an indication of average sediment fluxes (or residence
161 times) across basin components, will suggest whether or not disconnected
162 topographies are mirrored by slower sediment conveyance and evacuation rates.

163 In so doing, we investigate periglacial sub-basins dominated by creep of perennially-
164 frozen debris, sub-basins dominated by debris-flow transport, sub-basins in which
165 semi-alluvial channels are intermittently disturbed by debris slides and debris flows,

and sub-basins drained by purely alluvial channels. To expand the range of variability, we also examine the effects of regulated hydrologic and sedimentary pathways along Allitz Creek (Figure 2c). This latter aspect is relevant in mountain settings of the European Alps, where anthropogenic disturbance is pervasive. Finally, the study basins offer the opportunity to evaluate fluctuations in ^{10}Be-derived apparent denudation rates in the paraglacial context that led to the development of the Gadria fan between 12 and 6 kyr BP (Brardinoni *et al.,* 2018).

2. Setting

Gadria, Strimm and Allitz Creek are steep alpine headwater streams located in upper Vinschgau/Venosta Valley, South Tyrol, Italy (Figure 2). Elevation ranges from 3206 m a.s.l (Litzer Spitz) down to 822 m a.s.l. at the confluence of Allitz Creek with the Etsch/Adige River (Figure 2c). The area is amongst the driest within the Alps (Frei and Schaer, 1998), with mean annual precipitation in Silandro/Shlanders (698 m a.s.l.) of 502 mm (1921-2018) (Meteo Alto Adige, 2020).

Bedrock lithology is defined by polymetamorphic rocks of the Austroalpine Domain. Field-based geological surveys show that the area is crossed east-to-west by a tectonic contact separating the Mazia and Ötztal units (Ratschbacher *et al.,* 1989; Thöni, 1999) (Figure 3). Accordingly, lithologic variability is virtually identical in the two source basins. Most of the upper and mid portions of Gadria and Strimm basins are underlain by paragneiss and schist, with abundant metapegmatitic intrusions of the Mazia unit (Habler *et al.,* 2009). In the lower part, paragneiss and orthogneiss of the Ötztal unit, which in places have been reduced to phyllonite due to cataclastic deformation related to the Vinschger shear zone, outcrop. Quartz content is comparable across lithologies.

Lithologies in the upper part of the Gadria basin are particularly shattered, in correspondence of a sackung that occupies most part of the south-facing slopes (DSGSD in Figure 3). Geologic Strength Index values within the sackung is lower (35<GSI<45), in comparison to elsewhere in Gadria and across the Strimm basin (45< GSI<60) (Perina, 2012). The main body of the sackung, locally has dislocated the Mazia-Ötztal tectonic contact southward by over 100 m (Figure 3). In its upper portion, the sackung is covered by thick colluvial deposits and in places gives rise to badland-like topography. Such morphological features act as prominent sediment sources for debris flows that have dismantled large parts of the upper sackung body over postglacial timescales.

Gadria is a very active debris-flow basin consisting of four main colluvial channels that join the main stem southward. The catchment hosts a debris-flow monitoring station since 2011 (Comiti *et al.,* 2014; Coviello *et al.,* 2019). Strimm is a snowmelt-dominated fluvial system that originates on a decoupled hanging valley, and cascades through a tightly coupled relict trough. Four years of bedload monitoring in Strimm Creek have indicated that 80% of the fluvial transport is associated with high flows during the summer freshet, which occurs between early June and mid-July (Dell'Agnese *et al.,* 2015).

Allitz Creek is a trunk stream originating at the Gadria-Strimm confluence, downstream of a debris-flow retention basin (Figure 2c), which flows southward, along the axis of the Gadria fan, and joins the Adige River in proximity of the town of Laas/Lasa (Figure 2b). Both Strimm and Allitz Creek experience water diversion (i.e., from mid-April to mid-October) for irrigation of apple tree plantations that cover most of the fan. Water is intercepted at the outlet of Strimm Creek and in Allitz Creek, about 100m downstream of the retention basin (Figure 2c). By the end of July, Allitz

Creek at A1 is typically dry, while perennial stream flow is preserved at A2 through groundwater recharge.

All study reaches have a documented history of debris-flow disturbance and volumetric sediment transfer since 1998 (Figure 6 and Table 1) (Brardinoni *et al,* 2012; Cavalli *et al.,* 2017), with qualitative historical information dating as far back as to the 15th century.

To better characterize the spatial variability of geomorphic disturbance in the study basins, we have compiled a multi-temporal inventory of sediment sources, including shallow rapid failures (red and green polygons) and patches of chronic surficial erosion (orange polygons in Figure 5a). The inventory was compiled through visual inspection of: (i) four sequential sets of aerial photo stereo pairs (1959, 1969, 1982-1985, and 1992-95), ranging in nominal scale between 1:20,000 and 1:30,000; (ii) digital orthophotos (2000, 2006, 2008, and 2011); (iii) high resolution Bing Maps (http://www.bing.com/maps/) digital aerial photos (2012); and (iv) 2011 LiDAR shaded relief (i.e., generated from a 1-m gridded DTM). The inventory was complemented by fieldwork in the summer of 2010, 2011 and 2012, during which we measured the geometry of 28 shallow landslides across the Strimm basin. Landslide depth was found to be shallow, ranging between 20 and 45 cm, with a modal value of 35 cm. The event-based documentation on channel disturbance in conjunction with the multi-temporal inventory of sediment sources, have guided our selection of the ^{10}Be sampling locations within the Gadria and Strimm source basins (see Section 3).

3. Data collection and methods

3.1 Sampling strategy

In October 2012, we started collecting sand samples – each consisting of about 5 kg - from the active channel bed of the study streams at nine locations (Figures 2, to 5, and Tables 2 and S1). The sampling sites were selected based on the recent history of debris-flow disturbance (Figure 6) so that we could compare sub-basins drained by different transport/disturbance regimes and assess the sensitivity of [10Be] over time: colluvial (Montgomery and Buffington, 1997), semi-alluvial (or transitional), and purely alluvial channels (Halwas and Church, 2002).

In Strimm basin, we sampled at sites S1, S2, S3, S4 and S5 (Table 2). Site S1 is located in an ephemeral, decoupled channel reach that drains a periglacial sub-basin characterized by several intact and relict rock glaciers (Figure 2). Rock glaciers (violet polygons) are typically disconnected from shallow landslide activity (red and green polygons) as mapped between 1959 and 2012 (Figure 5a). Two lakes located within a relict hummocky moraine (yellow polygon) prevent glacigenic sediment from travelling down sampling site S2.

Site S2 lies within a permanent, decoupled, purely alluvial reach located at the downstream end of a major hanging valley (MHV in Figure 5a). Here, Strimm Creek is disconnected from shallow landslide erosion (red polygons) and deposition (green polygons in Figure 5a). Site S3 is situated in the distal-most reach of a colluvial tributary channel, where shallow mass wasting activity is common (Figure 5a) and that was last disturbed by a debris flow in 2010 (Figure 6). Sites S4 and S5 belong to two semi-alluvial reaches dominated by bedload transport that last experienced debris-flow activity in 2010. Site S5 differs from S4 in that it is coupled to a handful of small rotational slumps due to slope undercutting by debris flows.

In the Gadria basin, we sampled at site G1, at the headwaters of the most active (2008-2014, see Figure 6) debris-flow tributary that cuts through the sackung body,

and at site G2, along the Gadria main stem, about 50 m upstream of the retention basin. From July 2013, in order to evaluate the contribution of the two distal most tributaries G3 and G4 (Figure 4), we started collecting samples at site G3 in Gadria Creek (Table S1). In Allitz Creek, samples were collected at site A1, located 100 m downstream of the filter check dam that bounds the retention basin, and at site A2, about 30 m upstream from the confluence with the Adige River.

At sites S2, S4, S5; G2, G3, A1 and A2, we repeated the sand sampling one to three times between 2013 and 2014. Repetitions were made at high flows in July during snowmelt and at low flows in early October. In light of the paper objectives, the timing of repeated sampling was also dictated by the occurrence of debris flows. Specifically, samples collected at sites G2 and G3 in 2013 were collected after the event occurred on July 18 (Figure 6e). This event prevented foot access and sampling replications at site G1 for the rest of 2013 and in 2014. The small debris flow occurred on August 5, 2011 remobilized in-channel deposits, did not involve sediment recruitment from the dissected tributary G1 within the DSGSD area, and deposited 2000 m^3 in the retention basin (Table 1 and Figure 6d). This event did not produce detectable erosion on Gadria main stem (upstream of confluence with tributary G1) (cf., Figure 3b in Cavalli *et al.,* 2017).

3.2 ^{10}Be measurement

The collected samples were sieved for grain sizes fractions 0.250 – 1 mm and treated with heavy liquids to remove fractions above and below 2.62 – 2.68 g cm^{-3}. Subsequently, we used hydrogen peroxide (H_2O_2) to remove organic remains, to weather micas, and to corrode feldspar grains. This pre-treatment ensures a more efficient removal of micas and feldspars during the actual treatment of the samples with a mixture of fluosilicic and hydrochloric acid. When feldspar grains were no

longer visible, the samples were treated several times with hydrofluoric acid in order to remove atmospheric ^{10}Be.

The purified quartz samples were processed following the protocol described by von Blanckenburg *et al*. (1996). After adding a ^{9}Be carrier solution (Table 2), quartz was dissolved using concentrated HF and HNO_3. Separation of Be was achieved by anion and cation exchange and pH-sensitive precipitations, precipitated as $Be(OH)_2$ and transformed to BeO at 1000°C. The ^{10}Be/^{9}Be ratios of the ETH Zürich TANDY accelerator mass spectrometry (AMS) facility used the ETH AMS standard S2007N (^{10}Be/^{9}Be = 28.1 x 10^{-12} nominal (Christl and Kubik, 2013)), calibrated to the standard 07KNSTD (Nishiizumi *et al.,* 2007) with a ^{10}Be half-life of 1.387 Ma (Chmeleff *et al.,* 2010; Korschinek *et al.,* 2010). The subtracted procedural blank was 3.715 ± 0.276 x 10^{-15} (weighted mean ± 2σ, n=18) and represents mainly the ^{10}Be/^{9}Be ratio of the carrier solution. Finally, we propagated the blank error and analytical uncertainties to all ^{10}Be concentrations (Table 2).

3.3 Calculation of denudation rates and averaging time scales

We calculated catchment-wide denudation rates using the [10Be] in sand. We assumed that this concentration corresponds to a secular equilibrium between the gain by production and the loss by erosion on the hillslopes, while we did not take the radioactive decay of ^{10}Be into account (Brown *et al.,* 1995; Granger *et al.,* 1996; von Blanckenburg, 2006). Catchment-wide denudation rates can be calculated, in absence of debris-flow disturbance, using the following equation:

$$\varepsilon = \frac{1}{[\overline{N}]}\left(\frac{\overline{P}_{ni}}{\mu_n} + \frac{\overline{P}_{ms}}{\mu_{ms}} + \frac{\overline{P}_{ms}}{\mu_{ms}}\right) \qquad (1)$$

Where $\overline{P}_{ni}$, $\overline{P}_{ms}$, and $\overline{P}_{mf}$ are the average catchment-wide ^{10}Be production rates (at g^{-1} yr^{-1}) of neutrons, slow muons and fast muons, respectively, and $\mu_n = \left(\frac{\rho}{\Lambda_i}\right)$, where ρ is the average density of the eroded material (2.7 g cm^{-3}) and Λ_i is the effective attenuation length of neutrons, slow muons and fast muons (Λ_n~160, $\Lambda_{\mu s}$~1500 and $\Lambda_{\mu f}$~4320 g cm^{-2}; Braucher *et al.,* 2011).

The catchment-wide ^{10}Be production rates $\overline{P}$ were computed pixel per pixel on a LiDAR-derived, 2.5m-grid Digital Terrain Model (DTM) acquired by the Autonomous Province of Bolzano in 2005. The scaling to altitude and latitude was done following the scheme proposed by Stone (2000). Topographic shielding corrections were calculated using an ArcGIS-toolbox TopoShielding based on the method described by Codilean (2006). The components of nucleonic, stopped and fast muon production were separately computed and combined with the topographic shielding corrections, thus yielding separate mean values of the three production components. The value for the SLHL (sea level and high latitude)-spallation-production rate was 4.0 ±0.1 [at/gQz/y), which is lower than that by Balco *et al.* (2008), but agrees well with more recent calibration studies (e.g., Borchers *et al.,* 2015). The production rates for fast and stopped muons were taken from Heisinger *et al.* (2002). The basin-wide ^{10}Be production rate $\overline{P}$ was determined following a procedure proposed by Lupker *et al.* (2012), where locally calculated production rates on a pixel per pixel base were averaged. This procedure yielded a total production rate for the catchment that is about 10% higher than taking the mean altitude for the calculation. Since in this study we are comparing repeated samples of modern fluvial sands, we did not take into account the attenuation of cosmic rays through winter snow pack. We believe that the overall effect on the calculation of denudation rates is negligible (e.g., Schildgen *et al.,* 2005).

The time scales over which denudation rates are averaged (Table 3) are a function of the denudation rates themselves and were calculated by dividing the denudation rate by the absorption depth scale z*. This averaging time scale corresponds to the residence time in rock or soil within one absorption depth scale i.e., the top 0.6 m for bedrock, and about 1.0 m for soils (von Blanckenburg, 2006).

3.4 Structural geomorphic connectivity (IC Index)

The IC index (*IC = log Dup/Ddn*) is a spatially-distributed, geomorphometric index of structural geomorphic connectivity (Cavalli *et al.,* 2013). It is expressed at the raster cell scale by the logarithm of the ratio between an upslope component (*Dup*) and a downslope component (*Ddn*) (Figure 1). Given a raster cell in the DTM, *Dup* expresses the potential for downslope/stream routing of sediment produced (and/or available) in the relevant source basin. For a given raster cell, this potential is a function of average stream power and average surface roughness within the source basin draining to the raster cell. *Ddn* is a function of the ruggedness (i.e., surface roughness) of the flow path and the flow path length that sediment has to travel from the study raster cell in order to reach a given target (e.g., a channel cross section, a check dam). In this study, targets are the retention basin for Strimm and Gadria Creek, and the Adige River for Allitz Creek. IC values at sites A1 and A2 are shown for illustrative purpose only, as the index, in the absence of seasonal multi-temporal DTMs, cannot capture the local geomorphometric changes in response to variable rates of water diversion in time (Figure 2c). All variables for the calculation of the IC index are extracted from the above mentioned 2.5 m LiDAR-derived DTM. It is assumed that geomorphic activity between 2005 and 2012 (i.e., start of sampling campaigns) has not altered significantly the topographic structure of the sub-catchments and the spatial distribution of the IC index. This assumption is realistic,

considering the robustness of the IC index (Figure 1), and that no reconfiguration (i.e., blockage or obliteration) of the main sedimentary pathways was recorded along the drainage network between 2005 and 2011 (Cavalli *et al.,* 2017). By selecting Gadria and Strimm basins, we wish to build on prior work conducted on structural geomorphic connectivity, targeting the same sites where the IC index was first tested by Cavalli *et al* (2013). For ease of readability in log-log space, IC values are represented as IC* counterparts, where IC* = antilog IC (Section 4.3).

4. Results

We begin by presenting the spatial variability of [10Be] and apparent denudation rates on the first set of samples taken in October 2012 at nine study sites. Using error bars (i.e., blank error and analytical uncertainties) to evaluate statistically different ^{10}Be concentrations over time, we show the temporal variability of sampling replications conducted at seven of these sites. We finally examine the relationship between functional and structural connectivity by plotting [10Be] (and apparent CWDRs) against the IC index at each sampling location through time.

4.1 Spatial variability of samples collected in October 2012

The ^{10}Be-nuclide concentrations of the first sampling campaign (October 2012) span across two orders of magnitude, from 1865 ±562 (G1) to 226301 ±9103 at/gQtz (S1), which correspond to denudation rates ranging between 0.1 ±0.01 (S1) and 10.4 ±3.49 (G1) mm/yr (Figure 7 and Table 2). Along Strimm Creek, concentrations decrease (hence CWDRs increase) progressively downstream, from 226301 ±9103 at/gQtz at S1 -- in the blocky periglacial domain, characterized by long residence times (i.e., 5850 yr; Table 3) -- and 153887 ±6709 at/gQtz (CWDR = 0.14 ±0.02 mm/yr) at S2, in the decoupled fluvial channel reaches of the hanging valley floor,

down to 66201 ±8771 (0.31 ±0.05 mm/yr) at S4 and 54913 ±2797 at/gQtz (0.35 ±0.05 mm/yr) at S5, along the steep relict glacial trough, where residence times become shorter (i.e., 1650-1880 yr; Table 3) and Strimm Creek receives episodic sediment inputs from colluvial lateral tributaries, such as S3. Site S3 bears a concentration of 50191 ±4974 at/gQtz (0.38 ±0.06 mm/yr).

Compared to Strimm, samples taken in Gadria debris-flow channels carry an order of magnitude lower [10Be], and display a downstream increasing pattern. Sample G1, collected on a bedrock channel that cuts through highly erodible bedrock associated with the sackung, yielded 1865 ±562 at/gQtz (10.4 ±3.49 mm/yr), a value close to the blank level of the measurement that corresponds to very short residence time (i.e., 60 years). Sample G2, taken in Gadria Creek's distal most reach, which experiences debris-flow transport and deposition, as well as fluvial reworking, yielded 8421 ±1642 at/gQtz (1.78 ±0.51 mm/yr), with an estimated residence time of 330 years.

Samples collected along Allitz Creek, downstream of water diversions and downstream of the filter check dam, yielded [10Be] equal to 4284 ±1033 at/gQtz (3.96 ±1.17 mm/yr) at A1 and 9311 ±1661 (1.72 ±1.17 mm/yr) at A2. Interestingly, we note that [10Be] at A1 is significantly different than at G2. According to mixing theories (Granger et al., 1996; Binnie et al., 2006), a similar decrease cannot be explained over the short distance (i.e., 300 m) separating the two sites, especially when considering that the adjoining sediment signal exiting from Strimm Creek (site S5) should produce in A1 a comparably higher concentration than in G2.

4.2 Temporal variability

Sampling replications conducted in July 2013, October 2013 and July 2014 allow identifying three different trends in ^{10}Be concentrations (and CWDRs) (Figure 7).

Along Strimm Creek, which has not experienced significant debris-flow activity since 12 July 2010 (Table 1 and Figure 6c), we observe consistent ^{10}Be concentrations (and CWDRs) across the entire time series at each sampling site, with differences between replications plotting within error bars (i.e., from 640 to 11150 at/gQtz; Figure 7a and Table 2). Such consistency is observed both in purely alluvial (i.e., site S2) and in semi-alluvial channel reaches (i.e., sites S4 and S5).

At site G2, in samples collected after the debris flow occurred on July 18 2013, we observe a 4-fold progressive decline in [10Be] though October 2013 (i.e., concentrations in October 2012 are significantly different from those measured in July and October 2013). Concentration then remains constant (at least) through July 2014 (Figure 7a). At site G3, concentration exhibits an identical declining trend through October 2013, followed by a partial (not statistically significant) rebound to higher values in July 2014. At both sites, end members of the time series are significantly different (Figure 7a and Table 2).

In Allitz Creek, sampling replications at the two study sites (A1 and A2) show distinctive seasonal fluctuations in [10Be], with minima associated to samples collected in July, during snowmelt, and maxima corresponding to samples collected at low base flow, in early October (Figure 7a). At sites A1 and A2, the seasonal signal is statistically significant in terms of [10Be] (Figure 6a) and CWDRs (Figure 7b and Table 2), in contrast with the lack of seasonality observed in Strimm and Gadria. ^{10}Be concentrations in Allitz Creek tend to approach values characteristic of Strimm Creek during the snowmelt, and values more typical of Gadria Creek, when the snowmelt has ceased and episodic flushing of the catchments controls sediment flux.

Overall, the combination of apparent CWDRs and their temporal variability bound the time scales over which denudation rates are averaged. These range, theoretically,

433 between 60 and 330 years in the Gadria basin, between 1570 and 5850 years in
434 Strimm basin, and between 120 and 640 years in Allitz Creek (Table 3).

435 **4.3 Exploring the functional-structural connectivity nexus**

436 Gadria and Strimm are characterized by different structural connectivity, as depicted
437 by the spatial distributions of IC values (Figure 8a). In Strimm, we observe a relatively
438 more disconnected upper portion (i.e., blue-shaded parts delineate an upland
439 network of nested hanging valleys) and a lower one that is distinctively more
440 connected (i.e., orange-to-red shaded parts delineate a steep glacial trough ending
441 with a sub-vertical valley step) (Figures 4 and 8a). Sampling sites display a
442 downstream decreasing pattern of IC values in Gadria and an opposite increasing
443 one in Strimm, with site S3 (i.e., located in the colluvial tributary) plotting well above
444 the Strimm "main" relation (Figure 8b). Finally, Allitz sites exhibit intermediate values
445 (Figure 8b).

446 Analysis of the functional-structural connectivity nexus, where the functional
447 component is represented by [10Be], and the structural by IC values, shows that the
448 first set of samples (Oct 2012) collected in Gadria (empty diamonds) and Strimm
449 (empty triangles) describes a well-constrained, inverse relation (R^2 = 0.95; Figure
450 8c), which translates into a positive one for CWDRs (R^2 = 0.97; Figure 8d). Despite
451 the limited number of observations (n =7), which clearly prevents any reliable
452 statistical conjecture, conceptually, this tendency indicates that sub-catchments
453 characterized by a better-connected structure exhibit lower [10Be] (i.e., higher
454 apparent CWDRs) than those bearing higher IC index, and that a direct linkage
455 between structural and functional connectivity appears to hold over the time scales
456 considered (i.e., 10^2-10^3 years, Table 3). Interestingly, Allitz sites (empty squares in
457 Figures 8c-f), which display IC values slightly higher than those observed in Strimm,

458 but matched by much lower [10Be], tend to depart from the main relation described
459 by Gadria and Strimm sites, both in terms of [10Be] and CWDRs.

460 The temporal variability of ^{10}Be concentrations (and CWDRs) previously documented
461 in the 2013-14 sampling replications at sites G2 and G3 (filled diamonds in Figures
462 8e and 8f) leads to steeper, and more scattered Gadria-Strimm relations (filled
463 triangles and diamonds) in log-log space. Sampling replications in Allitz (filled
464 squares), plot away from the October 2012 Gadria-Strimm relation, but tend to fit the
465 2013-14 post-debris flow relation (filled symbols in Figures 8e and 8f).

466 **5. Discussion**

467 **5.1 Critical depth of erosion and the variability of [10Be] in time and space**

468 In a given (sub-) catchment, the types and intensity of geomorphic processes that
469 dominate hillslope sediment production and transfer are known to control the
470 observed [10Be] in sand samples taken at the outlet (Bierman and Steig, 1996;
471 Granger *et al.,* 1996; von Blanckenburg, 2006). For example, shallow, diffusional
472 processes like soil creep and sheetwash erosion tend to remove only the uppermost
473 (i.e., few centimetres) layer of material, which is typically enriched in ^{10}Be by efficient
474 spallogenic production. In contrast, rapid mass wasting processes, such as debris
475 slides and debris flows, can remove thicker layers of material at once (depending on
476 bedrock strength) and therefore can recruit sediment bearing a much lower nuclide
477 signature, due to lower muogenic production rates. Consequently, quantitative
478 information on depth of erosion on the slopes (local *vertical connectivity*) is crucial for
479 interpreting the variability of [10Be] in time and space, and relate them to ongoing
480 sediment dynamics (e.g., von Blanckenburg *et al.,* 2004; Tofelde *et al.*, 2018). In
481 particular, critical erosional depths, capable of exerting substantial shielding, are on

482 the order of 3 to 4 m, due to the transition from spallogenic to muogenic production
483 (Lal, 1991).

484 On such theoretical and empirical premises, in order to interpret the spatial and
485 temporal variability of [10Be] we used DoDs from sequential (2005-2011) LiDAR
486 DTMs to constrain the characteristic erosion depths across the Gadria and Strimm
487 catchments. Visual inspection of the DoD, in a period characterized by widespread
488 debris-flow activity in both study basins (Figures 6a, 6b and 6c), allows identifying
489 two distinctive styles of erosion: deeper in Gadria and shallower in Strimm (Figure 9).
490 In Gadria, deep patches of erosion (i.e., d > - 3m, red areas) are much bigger and
491 more widespread than in Strimm, where patches of somewhat comparable depth
492 (i.e., -1.5m < d < -3m, light red areas) occur in its lowermost sub-vertical reach
493 (Figure 9a). The remotely-based shallow style of erosion in Strimm basin, agrees with
494 field measurements of landslide depth (Figures 5b and 5c). In Gadria, deep patches
495 of erosion are clustered within the sackung perimeter, where bedrock has undergone
496 mechanical weakening and weathering (DSGSD in Figure 9b). This contrast is
497 confirmed by the frequency distributions of erosional depth in the two debris-flow
498 dominated tributaries draining to sampling sites G1 and S3 (Figure 10). The former
499 includes a much higher number of large erosion cells than the latter, with values that
500 locally can overcome 4 meters, thus implying the recruitment of shielded, low ^{10}Be
501 bearing material, induced by lower muogenic-dominated production.

502 Based on erosional depth information (Figures 9 and 10), debris-flow disturbance
503 history (Table 1 and Figure 6), and previous sampling time series conducted in
504 similar geomorphic settings (i.e., Kober *et al.*, 2019), we interpret [10Be] at G2 in
505 October 2012 (Figure 7a) as close to undisturbed (background) conditions, resulting
506 from a 26-month period with no significant debris-flow activity (Figure 6a-d). Sample

concentrations at G2 and G3 in July 2013, taken immediately after debris-flow occurrence, draw a statistically significant declining trend (Figure 7a), which we interpret as the consequence of low [10Be] delivered from G1 (i.e., d > -4m). This trend peaks in October 2013, possibly as a result of lag material detached from the debris-flow deposits emplaced three months earlier. In July 2014, we start observing some increase in [10Be] at site G3, even though within analytical uncertainty, which we speculate as possible sign of incipient recovery from debris-flow disturbance. Following this logic, relatively shallow erosional depths in Strimm basin, associated with the recruitment of sediment enriched in [10Be] by efficient spallogenic production, explain comparably higher and very stable [10Be] observed at Strimm sites across sampling replications.

Our findings agree with two recent multi-temporal studies indicating that "vertical connectivity" between spallogenic and muogenic domains, or the type and thickness of the sediment stores activated during storm events, may be critical to downstream sediment mixing by imparting sudden transient changes to local [10Be]. Specifically, post storm ^{10}Be concentrations have shown no significant change from pre-storm analogues in headwater systems (i.e., 0.53 < drainage area (DA) < and 10 km^2) of the Colorado Front Range, where sediment transfer involved shallow (< 1 m) colluvial and alluvial sedimentary fills, characterized by hundreds to a thousand years residence times (Foster and Anderson, 2016). Conversely, repeated sampling conducted in fluvial reaches of the upper Aare catchment, Central Swiss Alps, indicated that sediment inputs associated with a series of large (10^4-10^5 m^3) debris flows, recruiting material from thick (down to 20 m erosional depths) post-LGM colluvial deposits in tributary catchments (DA = 4 km^2), could lower [10Be] in the

alluvial main stem (DA = 69 km^2) by a factor of two, with a perturbation lasting for 2 to 4 years (Kober *et al.,* 2012; 2019).

A similar effect on [10Be] was observed in two samples collected by Savi *et al*. (2014) in 2010 in the Zielbach catchment, located 30 km east of Gadria-Strimm. In that case, two large debris flows originating from steep tributaries (DA = 0.8-1.5 km^2) occurred in 2008 (70,000 m^3) and 2009 (23,000 m^3) depressed [10Be] by a factor of two along the Zielbach main channel (DA = 32 km^2), compared to pre disturbance conditions (Norton *et al.,* 2011).

In this context, our work extends prior knowledge about the magnitude and duration of debris-flow occurrence on [10Be] and CWDR. By targeting disturbance effects in the colluvial reaches of a tributary catchment (DA_{G2} = 5.8 km^2; DA_{G3} = 3.4 km^2) – as opposed to fluvial reaches of a larger receiving alluvial system – we show that an 8,000 m^3 event was enough to depress [10Be] by a factor of four, and accordingly elevate apparent denudation rates, for at least 2 years.

The debris-flow perturbation induced on Gadria's [10Be] affects the slope of the functional-structural connectivity relation, which becomes steeper and noisier, compared to that described by samples collected in October 2012 (Figures 8c-e). Despite the limited number of seasonal samples (n = 7), which prevents pursuing statistical significance, our findings suggest that the IC index, especially in undisturbed conditions, might be a suitable metric for constraining first-order estimate of denudation rates and for evaluating structural connectivity over centennial to millennial time scales, provided that in the meanwhile sudden catastrophic events, for example a rock avalanche (e.g., Frattini *et al.,* 2016), have not changed the main sedimentary pathways within a given (sub-) catchment. On the contrary, we argue that more scattered IC-[10Be] relations, may point to transient disconnected

556 geomorphic configurations (e.g., a rock glacier advance that has progressively
557 blocked a mountain stream, or the progressive obliteration of a moraine or a landslide
558 dam), or to anthropogenic disturbance, where scatter is introduced by high variability
559 in [10Be] for given IC values i.e., the trend described by Allitz and Gadria (2013-14)
560 data points in Figure 7. To corroborate our interpretations, further sampling
561 replications are needed in other sites with known disturbance history and available
562 high-resolution digital topography.

563 To provide broader context to the IC index (Figure 11a), we compare its performance
564 to that of other metrics previously used to evaluate topographic controls on TCN-
565 derived denudation rates. These include basin-mean slope (e.g., Binnie et *al.,* 2007)
566 and basin-mean normalized channel steepness index (K_{sn}) (e.g., DiBiase *et al.,*
567 2010). Both slope (Figure 11b) and steepness index (Figure 11c), as expected,
568 display positive correlation with denudation rate. However, when considering close to
569 undisturbed conditions (i.e., samples collected in October 2012; empty symbols),
570 they perform comparatively worse than the IC index.

571 Mean-basin slope is particularly noisy across Strimm Creek (empty triangles in Figure
572 11b), indicating that this simple topographic variable is not a suitable metric for
573 denudation rates in complex mountain topography characterized by nested hanging
574 valleys and valley steps. By contrast, the steepness index does well in Strimm Creek,
575 but appears problematic for (i) discriminating between debris-flow disturbed and
576 undisturbed conditions in Gadria, since filled and empty diamonds lie along the same
577 k_{sn} invariant relation (Figure 11c); and for (ii) identifying anthropogenic disturbance,
578 since Allitz samples (squares) plot on top of Gadria samples (diamonds in Figure
579 11c).

This outcome should not surprise, since the steepness index was developed to study active unglaciated mountain ranges, and assess tectonic forcing on river long profile evolution (Wobus *et al.,* 2006). Accordingly, it has been successfully applied over larger spatial scales – for example, DiBiase *et al.* (2010) excluded basins < 2 km^2 – to evaluate the topographic characteristics of the drainage network, as opposed to assess basin-wide structural connectivity. Following this logic, the IC index better performance may be due to its architecture, refined for specific usage with high-resolution digital topography over steep complex topography (Cavalli *et al.,* 2013), and conceived to capture both the lateral (hillslope-channel) and longitudinal (along channel) components of structural connectivity.

5.2 Anthropogenic-driven seasonal variability

Seasonal water diversion, together with a filter check dam and a retention basin located at the Gadria-Strimm confluence (Figure 2c) may affect in Allitz Creek the mixing of high [10Be] sediment sourced by Strimm basin with low counterpart from Gadria (Tables 2 and 3). To evaluate the combination of these man-made structures, we model sediment mixing in Allitz Creek at sites A1 and A2, following the procedure proposed by Binnie *et al.* (2006) (Figure 12). This procedure combines nuclide balance and evaluation of sediment fluxes upstream and downstream of a confluence. Based on the nuclide balance, the downstream concentration must be comprised between the concentrations of the two upstream segments (grey envelope in Figure 12), assuming no admixing of other sediment sources occurs. Average sediment flux in each source basin is calculated by converting nuclide concentration to denudation rate, multiplied by the corresponding basin area. The ratio between the two denudation rates yields the relevant sediment proportion envelope (vertical hatched area in Figure 12). Sediment mixing can then be assessed graphically, by

plotting the nuclide concentration of the samples collected below the confluence. Adequate sediment mixing is achieved when the intersection area of the downstream (green and/or pink envelopes In Figure 12) and upstream (grey envelope) 10Be concentrations overlaps with the sediment proportion (vertical hatched area).

Mixing conditions at the confluence are challenging, since Gadria delivers sediment chiefly via frequent debris flows and fluvial reworking, while Strimm through snowmelt-dominated transport regime (Dell'Agnese *et al.,* 2015). Indeed, the degree of mixing of sediments from Strimm and Gadria basin appears to be seasonal (Figure 12). In the fall samples, sediments tend to be better mixed at site A2 (4.2 km downstream of the confluence) in contrast to site A1 (0.1 km downstream) (Figure 12a and 12c). The trend is reversed during summer sampling, where the sediment at site A1 is better mixed than further downstream at site A2 (Figure 12d). This counter-intuitive seasonal behavior, which is also preserved in October 2013 (Figure 12c), despite debris-flow occurrence on July 18th (Figure 5e), has not been observed before (e.g., Binnie *et al.,* 2006, Savi *et al.,* 2014).

In consideration of the observed inconsistent mixing, and taking into account the possible roles played by the retention basin and by seasonal water diversion on Allitz Creek sediment transport regime, we explain this seasonal behaviour with a combination of anthropogenic "switchers" and "sediment reservoirs" that alter the natural hydrologic and sedimentary pathways, hence the sediment mixing (Figure 13a). In turn, these changes translate in altered cosmogenic mixing and biased CWDRs. In particular, according to field observations the role of the retention basin is two-fold, on one hand it disconnects Allitz Creek permanently from most of debris-flow sediment inputs (i.e., 85-90%), on the other, it functions as a temporary sediment store that chronically releases sand-sized material to Allitz Creek via fluvial

reworking of the debris-flow deposits. Considering that the retention basin was emptied artificially in the fall of 2010, and given the lack of debris-flow activity in Strimm Creek between 2011 and 2014 (Figure 6), one can assume that the sediment stored behind the filter check dam derives chiefly from the Gadria basin.

With the above premises in mind, we interpret the high TCN concentrations in July, when Strimm water diversion is proportionally minor (i.e., between 20 and 40% of the natural streamflow), as the effect of sediment with high [10Be] sourced by Strimm Creek, which crossing the retention basin overwhelms the lower [10Be] signal originating from Gadria Creek. Likely, Strimm dominance over Gadria is amplified by its pronounced snowmelt regime that typically lasts from late spring to mid summer (Dell'Agnese *et al.*, 2015).

By contrast, at the end of the snowmelt, when water diversion intercepts 70% to 100% of the total flow and Strimm Creek's contribution is virtually switched off, the signal in Allitz Creek is dominated by sediment with low [10Be] from Gadria Creek, either sourced by summer debris flows or by fluvial reworking of older deposits in the retention basin (Figure 13a). A similar water shortage in Allitz Creek, which can start as early as late July and last till early October, brings about insufficient mixing in the vicinity of the Gadria-Strimm confluence (i.e., A1) that propagates for some kilometres down to the confluence with the Adige River (i.e., A2; Figure 12). We hypothesize that in natural conditions the temporal variability of concentrations along Allitz Creek would be dominated by the magnitude-frequency of debris flows in transit in Gadria Creek, with a possible dampening of the Gadria signal during snowmelt (Figure 13b).

5.3 Short-term perturbations in the post-LGM context

In the Gadria-Strimm system, existing information on debris-flow deposition at the retention basin (Comiti *et al.,* 2014; Cavalli *et al.,* 2017; Coviello *et al.,* 2019) allow constraining, between 1998 and 2017, a sediment yield of about 12,000 m^3/yr ± 10% at the Gadria outlet. This annual average, although obtained from systematic measurements made in the last 20 years only, is in line with frequency of sediment mechanical removal when capacity (~70, 000 m^3) of the retention basin is periodically reached, since the 1970's, when the filter check-dam was built. The additional contribution of Strimm Creek is estimated to vary between 15 and 20% of Gadria's yield (Dell'Agnese *et al.,* 2015; Cavalli *et al.,* 2017). These data, in conjunction with postglacial sedimentation rates of the Gadria fan (12-6 kyr BP), allowed depicting a long-term paraglacial perturbation in sediment outflow (Brardinoni *et al.,* 2018), as reported in Figure 14b. In this context, we are going to evaluate the significance of short-term perturbations observed in Gadria and Allitz Creek ^{10}Be denudation rates, with special reference to sites G2 (Gadria outlet) and A1 (downstream of the filter check-dam) (Figure 14a).

The variability at G2 has been explained by the transit of a debris flow that involved recruitment of sediment within the sackung perimeter beyond critical depth of spallogenic production, and as such characterized by drastically lower [10Be]; the trend in A1 has been interpreted as the result of man-altered hydrologic and sedimentary pathways interacting with Strimm's snowmelt-dominated transport regime (Figure 13).

Considering the decadal to centennial time scales over which ^{10}Be denudation rates are integrated (Table 3), the 1998-2017 sediment yield at Gadria outlet will be used here as an independent (first-order approximation) term of comparison for corresponding denudation rates. Similarly, sediment yield obtained from Gadria fan

679 sedimentation rates, will be used as a long-term reference against which evaluate the
680 significance of observed fluctuations in ^{10}Be denudation rates.

681 Translation of denudation rates (Figure 14a) into sediment yield (Figure 14b and
682 Table 3) – with all the inherent limitations that using non-steady, episodic ^{10}Be
683 denudation rates may involve – indicates that corresponding sediment fluxes at the
684 Gadria outlet (G2) start at 10,300 ±2,900 m^3/yr in October 2012 (hence substantially
685 matching sediment yield measured between 1998 and 2017) and would skyrocket to
686 30,000 m^3/yr (July 2013) and over 43,000 ±12,100 m^3/yr (October 2013 and July
687 2014) after the occurrence of a debris flow (Table 3). Despite the differences in
688 integration time scales (strictly 20 vs 80+ years), these figures reinforce our
689 interpretation that ^{10}Be concentrations in October 2012 would represent
690 contemporary background (close to undisturbed) conditions, and that a period of 26
691 months (i.e., July 2010-Oct 2012) can suffice to offset the relevant debris-flow
692 perturbation (i.e., bias) in ^{10}Be denudation rate. Furthermore, in the October 2012
693 samples, the Gadria-Strimm sediment yield ratio (supplementary Table S2) matches
694 the contemporary 5:1 yield ratio. On the contrary, sediment yields of 30,000 to 43,000
695 m^3/yr in Gadria are considered unrealistic (not sustainable) over averaging time
696 scales of 80 to 100+ years (Table S2 and Table 3) and are more in line with fluxes
697 inferred for the Early Holocene (Figure 14b). Overall, considering the time scales
698 examined in this work by means of geophysical surveying and borehole logging of
699 the Gadria fan, contemporary monitoring of sediment flux, and analysis of [10Be] in
700 fluvial sands, rates of sediment transfer in the Mid to Late Holocene remain
701 undefined (Figure 14b).

702 In terms of topography, the Gadria and Strimm basins best exemplify how complex
703 and diverse the degree of glacial inheritance can be, since these two adjacent basins

share the same Quaternary history and hydro-meteorological forcing. If on one hand, the Strimm basin hosts a wide range of currently-active geomorphic process domains (i.e., periglacial, colluvial, and fluvial), whose topographic signatures are for the most part still largely conditioned by the glacial palimpsest (Figure 2; cf. Strimm long profile in Figure 4). In Gadria Creek, we observe the characteristic "unglaciated" debris-flow topographic signature in the area-slope representation of all four tributaries (i.e., two power-laws relations with an inflection point around 1 km^2; Stock and Dietrich, 2003) (Figure 14c and Figure S1), thus suggesting that the topography of this catchment has obliterated the imprinting of Pleistocene glaciations (Brardinoni and Hassan, 2006). We argue that this fast regained "unglaciated" structure, which results from at least 6,000 years of intense debris-flow activity (Brardinoni *et al.,* 2018), has been aided by the structural conditioning of the sackung on bedrock strength. Accordingly, the sackung appears to hold (and have held) a prominent role at several levels: (i) on contemporary sediment dynamics by facilitating critical erosional depths and high debris flow activity, which induce perturbations on ^{10}Be denudation rates; (ii) on decadal to millennial time scales, by promoting high structural connectivity in Gadria; and (iii) on post-LGM landscape evolution, by facilitating accelerated obliteration of the glacial topographic signature.

6. Conclusions

By employing seasonal sampling of ^{10}Be, we show that climate and geomorphic perturbations in sediment delivery control ^{10}Be concentrations in stream sediment. This effect is amplified by the anthropogenic alteration of the basin's hydrology. Our findings indicate that in steep headwater systems the timing of TCN sampling, in relation to seasonal and inter-annual perturbations, can be critical for inferring a representative average CWDR at a point, and that these perturbations may result as

729 the combined effects of glacial landscape structure on geomorphic connectivity,
730 DSGSD conditioning and debris-flow occurrence.

731 In particular, we document the effects of debris-flow disturbance on [10Be] at the
732 Gadria sampling sites, where we argue that the weakening in bedrock strength
733 imparted by the DSGSD, leads to high(er) depth of erosion on the slopes (vertical
734 connectivity) and efficient sediment evacuation via high lateral and longitudinal
735 structural connectivity (i.e., highest IC values). Debris flows, by picking up sediment
736 below critical depth for spallogenic production (e.g., > 3 m), can perturb and elevate
737 apparent denudation rates at the basin outlet up to a factor of 4.

738 Our data show that this perturbation can last for at least 2 years, but we do not rule
739 out longer recovery times for colluvial channels scoured by larger debris flows.
740 Conversely in Strimm Creek, where bedrock strength is higher, shallower erosional
741 depths are associated with steady ^{10}Be-derived denudation rates at the outlet.
742 Downstream of the Strimm-Gadria confluence, we observe 2- to 4-fold seasonal
743 fluctuations in apparent denudation rates, which we ascribe to the combined effects
744 of regulated hydrologic and sedimentary pathways.

745 Collectively, ^{10}Be monitoring in the study basins suggests that, especially in close to
746 undisturbed conditions, denudation rates correlate directly with IC index, and that
747 implicitly, an additional dimension comes into play: the active depth of the sediment
748 stores that are involved during storm events. This correlation indicates that a strong
749 functional-structural connectivity nexus can be preserved across 10^2-10^3yr, and that
750 the IC index (in close to undisturbed conditions) may be regarded as a suitable metric
751 for constraining envelopes of denudation rates and for evaluating structural
752 connectivity. The index performs comparably better than other metrics (i.e., mean
753 slope and mean k_{sn}) previously used to assess topographic controls on denudation

rates in active unglaciated ranges. In this sense, further testing via multi-temporal sampling in other steep geomorphic settings is needed.

From the landscape evolution standpoint of high relief, polymetamorphic terrain, our work further supports that Deep-Seated Gravitational Slope Deformations act as effective agents of postglacial topographic adjustment (Agliardi *et al.,* 2013), showing that such features (either active or relict), by fostering intense and sustained debris-flow sediment flux over millennia, can lead to the rapid obliteration of the glacial topographic imprint.

7. Acknowledgements

Cosmogenic analysis was funded by SNF through Project 200021_135317/1, as part of RG PhD work. FB was funded through a University of Bologna grant. Geologic data acquisition and analysis were funded by the Autonomous Province of Bolzano, Ufficio Geologia e Prove Materiali through the CARG Project. DoD data were kindly provided by the Free University of Bozen-Bolzano and the CNR IRPI. Field assistance by Emilio Perina, Giulia Bonfanti and Giacomo Falsitta is greatly acknowledged. We thank two anonymous reviewers and the AE for providing very constructive and detailed comments on the manuscript.

8. Conflict of Interest Statement

The authors declare that there is no conflict of interest.

9. Data Availability Statement

The data sets used and/or analyzed during the current study are available from the corresponding author on reasonable request.

10. References

Agliardi, F., Crosta, G.B., Frattini, P., and Malusà, M.G. (2013) Giant non-catastrophic landslides and the long-term exhumation of the European Alps. *Earth and Planetary Science Letters*, 365, 263-274.

Alfonso-Torreño, A., Comez-Gutierrez, A., Schnabel, S., Lavado Contador, J.F., de Sanjose Blasco, J.J., and Sanchez Fernandez, M. (2019) sUAS, SfM-MVS photogrammetry and a topographic algorithm method to quantify the volume of sediments retained in check-dams. *Science of the Total Environment*, 678, 369–382.

Bierman, P., and Steig, E. J. (1996) Estimating rates of denudation using cosmogenic isotope abundances in sediment. *Earth Surface Processes and Landforms*, 21, 125-139.

Binnie, S. A., Phillips, W. M., Summerfield, M. A., and Fifield, L. K. (2006) Sediment mixing rapidly and basin-wide cosmogenic nuclide analysis in eroding mountainous environments. *Quaternary Geochronology*, 1, 4-14.

Binnie, S.A., Phillips, W.M., Summerfield, M.A., and Fifield, L.K. (2007) Tectonic uplift, threshold hillslopes, and denudation rates in a developing mountain range. *Geology*, 35, 743-746.

von Blanckenburg, F. (2006) The control mechanisms of erosion and weathering at basin scale from cosmogenic nuclides in river sediment. *Earth and Planetary Science Letters*, 242, 224-239.

von Blanckenburg, F., Hewawasam, T., and Kubik, P. W. (2004) Cosmogenic nuclide evidence for low weathering and denudation in the wet, tropical highlands of Sri Lanka. *Journal of Geophysical Research: Earth Surface*, 109(F3).

Borselli, L., Cassi, P., and Torri, D. (2008) Prolegomena to sediment and flow connectivity in the landscape: a GIS and field numerical assessment. *Catena*, 75, 268–277.

Bracken, L.J., Turnbull, L., Wainwright, J., and Bogaart, P. (2015) Geomorphic connectivity: a framework for understanding sediment transfer at multiple scales. *Earth Surface Processes and Landforms*, 40, 177–188.

806 Brardinoni, F., Hassan, M.A. (2006) Glacial erosion, evolution of river long-profiles,
807 and the organization of process domains in mountain drainage basins of coastal
808 British Columbia. *Journal of Geophysical Research: Earth Surface*, 111, F01013.

809 Brardinoni, F., Church, M., Simoni, A., and Macconi, P. (2012) Lithologic and glacially
810 conditioned controls on regional debris-flow sediment dynamics. *Geology*, 40, 455-
811 458.

812 Brardinoni, F., Hassan, M. A., Rollerson, T., and Maynard, D. (2009) Colluvial
813 sediment dynamics in mountain drainage basins. *Earth and Planetary Science*
814 *Letters*, 284, 310-319.

815 Brardinoni, F., Picotti, V., Maraio, S., Bruno, P.P., Cucato, M., Morelli, C., and Mair,
816 V. (2018) Postglacial evolution of a formerly glaciated valley: Reconstructing
817 sediment supply, fan building and confluence effects at the millennial time
818 scale. *Geological Society of America Bulletin*, 130, 1457-1473.

819 Brown, E. T., Stallard, R. F., Larsen, M. C., Raisbeck, G. M., and Yiou, F. (1995)
820 Denudation rates determined from the accumulation of in situ-produced Be-10 in the
821 Luquillo experimental forest, Puerto-Rico. *Earth and Planetary Science Letters*, 129,
822 193-202.

823 Brunsden, D., and Thornes, J.B. (1979) Landscape Sensitivity and Change.
824 *Transactions of the Institute of British Geographers*, 4, 463–484.

825 Caine, N., and Swanson, F.J. (1989) Geomorphic coupling of hillslope and channel
826 systems in two small mountain basins. *Zeitschrift fur Geomorphologie*, 33, 189–203.

827 Cavalli, M., Trevisani, S., Comiti, F., and Marchi, L. (2013) Geomorphometric
828 assessment of spatial geomorphic connectivity in small Alpine catchments.
829 *Geomorphology*, 188, 31-41.

830 Cavalli, M., Goldin, B., Comiti, F., Brardinoni, F., and Marchi, L. (2017) Assessment
831 of erosion and deposition in steep mountain basins by differencing sequential digital
832 terrain models. *Geomorphology*, 291, 4–16.

833 Chartin, C., Evrard, O., Laceby, J.P., Onda, Y., Ottle, C., Lefevre, I., and Cerdan, O.
834 (2017) The impact of typhoons on sediment connectivity: Lessons learnt from

835 contaminated coastal catchments of the Fukushima Prefecture (Japan). *Earth*
836 *Surface Processes and Landforms*, 42, 306‐317.

837 Church, M. (1995) Geomorphic response to river flow regulation: Case-studies and
838 time-scales. *Regulated Rivers: Research & Management*, 11, 3-22.

839 Church, M., and Slaymaker, O. (1989) Disequilibrium of Holocene Sediment Yield in
840 Glaciated British-Columbia. *Nature*, 337, 452-454.

841 Comiti, F., Marchi, L., Macconi, P., Arattano, M., Bertoldi, G., Borga, M., Brardinoni,
842 F., Cavalli, M., D'Agostino, V., Penna, D., and Theule, J. (2014) A new monitoring
843 station for debris flows in the European Alps: first observations in the Gadria basin.
844 *Natural Hazard*, 73, 1175-1198.

845 Coviello, V., Theule, J.I., Marchi, L., Comiti, F., Crema, S., Cavalli, M., Arattano, M.,
846 Lucía, A., and Macconi, P. (2019) *Deciphering sediment dynamics in a debris-flow*
847 *catchment: insights from instrumental monitoring and high-resolution topography*. In:
848 Kean, J.W., Coe, J.A., Santi, P.M. and Guillen, B.K., eds. 7th International
849 Conference on Debris-Flow Hazards Mitigation: 103-110.

850 Dadson, S., Hovius, N., Chen, H., Dade W.B., et al., 2004. Earthquake-triggered
851 increase in sediment delivery from an active mountain belt. *Geology*. 8, 733-736.

852 Dell'Agnese, A., Brardinoni, F., Toro, M., Mao, L., Engel, M., and Comiti, F. (2015)
853 Bedload transport in a formerly glaciated mountain catchment constrained by particle
854 tracking. *Earth Surface Dynamics*, 3, 527–542.

855 Delunel, R., Van der Beek, P. A., Bourlès, D. L., Carcaillet, J., and Schlunegger, F.
856 (2014) Transient sediment supply in a high-altitude Alpine environment evidenced
857 through a ^{10}Be budget of the Etages catchment (French Western Alps). *Earth*
858 *Surface Processes and Landforms*, 39, 890-899.

859 DiBiase, R.A, Whipple, K.X., Heimsath, A.M., and Ouimet, W.B. (2010) Landscape
860 form and millennial erosion rates in the San Gabriel Mountains, CA. *Earth and*
861 *Planetary Science Letters*, 289, 134–144.

862 Foster, M.A., and Anderson, R.S. (2016) Assessing the effect of a major storm on
863 ^{10}Be concentrations and inferred basin-averaged denudation rates. *Quaternary*
864 *Geochronology*, 34, 58–68.

865 Frattini, P., Riva, F., Crosta, G.B., Scotti, R., Greggio, L., Brardinoni, F., and Fusi, N.
866 (2016) Rock-avalanche geomorphological and hydrological impact on an alpine
867 watershed. *Geomorphology*, 262, 47–60.

868 Frei, C., and Schär, C. (1998) A precipitation climatology of the Alps from high-
869 resolution rain-gauge observations. *International Journal of Climatology*, 18, 873-900.

870 Fryirs, K. A., Brierley, G. J., Preston, N. J., and Kasai, M. (2007) Buffers, barriers and
871 blankets: The (dis)connectivity of catchment-scale sediment cascades. *Catena*, 70,
872 49-67.

873 Granger, D. E., Kirchner, J. W., and Finkel, R. (1996) Spatially averaged long-term
874 erosion rates measured from in situ-produced cosmogenic nuclides in alluvial
875 sediment. *Journal of Geology*, 104, 249-257.

876 Granger, D. E., Lifton, N. A., and Willenbring, J. K. (2013) A cosmic trip: 25 years of
877 cosmogenic nuclides in geology. *Geological Society of America Bulletin*, 125, 1379-
878 1402.

879 Grant, G. (2012) *The geomorphologic responses Gravel-bed rivers to Dams:*
880 *Perspectives and prospects.* Chapter 15, 165-181. In: Church, M.; Biron, P. M.; Roy,
881 A. G., eds. Gravel-bed rivers: processes, tools, environments. Chichester, UK: John
882 Wiley & Sons, Ltd.

883 Habler, G., Thoni, M., and Grasemann, B. (2009) Cretaceous metamorphism in the
884 Austroalpine Matsch Unit (Eastern Alps): The interrelation between deformation and
885 chemical equilibration processes. *Mineralogy and Petrology*, 97, 149-171.

886 Halwas, K. L., and Church, M. (2002). Channel units in small, high gradient streams
887 on Vancouver Island, British Columbia. *Geomorphology*, 43, 243– 256.

888 Heckmann T, Cavalli M, Cerdan O, Foerster S, Javaux M, Lode E, Smetanova A,
889 Vericat D, and Brardinoni F. (2018) Indices of geomorphic connectivity: opportunities,
890 challenges and limitations. *Earth-Science Reviews*, 187, 77-108.

891 Hinderer, M., Kastowski, M., Kamelger, A., Bartolini, C., and Schlunegger, F. (2013)
892 River loads and modern denudation of the Alps – A review. *Earth-Science Reviews*.
893 118, 11–44.

894 Kirchner, J.W., Finkel, R.C., Riebe, C.S., Granger, D.E., Clayton, J.L., King, J.G., and
895 Megahan, W.F. (2001) Mountain erosion over 10 yr, 10 ky, and 10 my time scales.
896 *Geology*. 29, 591–594.

897 Kober, F., Hippe, K., Salcher, B., Ivy-Ochs, S., Kubik, P. W., Wacker, L., and Hählen,
898 N. (2012) Debris-flow-dependent variation of cosmogenically derived catchment-wide
899 denudation rates. *Geology*, 40, 935-938.

900 Kober, F., Hippe, K., Salcher, B., Grischott, R., Zurfluh, R., Hajdas, I.,
901 Wacker, L., Christl, M., and Ivy-Ochs, S. (2019) Postglacial to Holocene landscape
902 evolution and process rates in steep alpine catchments. *Earth Surface Processes*
903 *and Landforms*, 44, 242-258.

904 Korup, O. (2012) Earth's portfolio of extreme sediment transport events. *Earth-*
905 *Science Reviews*, 112, 115-125.

906 Lal, D. (1991) Cosmic ray labeling of erosion surfaces: in situ nuclide production
907 rates and erosion models. *Earth and Planetary Science Letters*, 104, 424-439.

908 Lu, X., Li, Y., Washington-Allen, R.A., and Li, Y. (2019) Structural and
909 sedimentological connectivity on a rilled hillslope. *Science of the Total Environment*,
910 655, 1479-1494.

911 Meteo Alto Adige, (2020) http://www.provincia.bz.it/meteo/download/09700MS-PS-
912 Silandro-Schlanders.pdf (webpage accessed on July 1st 2020).

913 Milliman, J. D., and Farnsworth, K.L. (2011) *River Discharge to the Coastal Ocean*.
914 Cambridge, UK: Cambridge University Press.

915 Montgomery, D. R., and Buffington, J.M. (1997) Channel-reach morphology in
916 mountain drainage basins. *Geological Society of America Bulletin*, 109, 596– 611.

917 Neilson, T. B., Schmidt, A. H., Bierman, P. R., Rood, D. H., and Gonzalez, V. S.
918 (2017) Efficacy of in situ and meteoric 10Be mixing in fluvial sediment collected from
919 small catchments in China. *Chemical Geology*, 471, 119-130.

920 Niemi, N. A., Oskin, M., Burbank, D. W., Heimsath, A. M., and Gabet, E. J. (2005)
921 Effects of bedrock landslides on cosmogenically determined erosion rates. *Earth and*
922 *Planetary Science Letters*, 237, 480-498.

Norton, K.P., von Blanckenburg, F., DiBiase, R., Schlunegger, F., and Kubik, P.W. (2011) Cosmogenic 10Be-derived denudation rates of the Eastern and Southern European Alps. *International Journal of Earth Science*, 100, 1163-1179.

Perina, E. (2012) *Geomorfologia e aspetti geomeccanici del sistema Gadria-Strimo, Val Venosta* [M.S. thesis]: Dipartimento di Scienze Geologiche e Geotecnologie, Università Milano-Bicocca, 270 pp.

Ratschbacher, L., Frisch, W., Neubauer, F., Schmid, S.M., and Neugebauer, J. (1989) Extension in compressional orogenic belts: the eastern Alps. *Geology*, 17, 404–407.

Reiners, P. W., and Brandon, M. T. (2006) Using thermochronometry to understand orogenic erosion. *Annual Reviews in Earth Planetary Science*, 34, 419-466.

Savi, S., Norton, K., Picotti, V., Brardinoni, F., Akcar, N., Kubik, P. W., Delunel, R., and Schlunegger, F. (2014) Effects of sediment mixing on Be-10 concentrations in the Zielbach catchment, central-eastern Italian Alps. *Quaternary Geochronology*, 19, 148-162.

Sougnez, N., van Wesemael, B., and Vanacker, V. (2011) Low erosion rates measured for steep, sparsely vegetated catchments in southeast Spain. *Catena*, 84, 1–11.

Stock, J., and Dietrich, W. E. (2003) Valley incision by debris flows: Evidence of a topographic signature. *Water Resources Research*, 39, 4.

Stutenbecker, L., Delunel, R., Schlunegger, F., Silva, T.A., Šegvić, B., Girardclos, S., Bakker, M., Costa, A., Lane, S.N., Loizeau, J-L., Molnar, P., Akçar, N., and Christl M. (2018) Reduced sediment supply in a fast eroding landscape? A multi-proxy sediment budget of the upper Rhône basin, Central Alps. *Sedimentary Geology,* 375, 105–119

Thöni, M. (1999) A review of geochronological data from the Eastern Alps. *Schweizerische Mineralogische und Petrographische Mitteilungen,* 79, 209–230.

Thorn, C. E., and Rhoads, B. L. (1996) *The scientific nature of geomorphology: proceedings of the 27th Binghamton Symposium in Geomorphology, held 27-29 September, 1996*. Wiley.

Tofelde, S., Duesing, W., Schildgen, T., Wickert, A. D., Wittmann, H., Alonso, R. N., and Strecker, M. (2018) Effects of deep-seated versus shallow hillslope processes on cosmogenic 10Be concentrations in fluvial sand and gravel. *Earth Surface Processes and Landforms*, 43, 15, 3086-3098.

Vanacker, V., von Blanckenburg, F., Govers, G., Molina, A., Poesen, J., Deckers, J., and Kubik, P. (2007) Restoring dense vegetation can slow mountain erosion to near natural benchmark levels. *Geology*, 35, 303-306.

Wobus, C., Whipple, K.X., Kirby, E., Snyder, N., Johnson, J., Spyropolou, K., Crosby, B., and Sheehan, D. (2006) Tectonics from topography: procedures, promise, and pitfalls. *Geological Society of America Special Papers*, 398, 55–74.

Yanites, B.J., Tucker, G.E., and Anderson, R. (2009) Numerical and analyticalmodels of cosmogenic radionuclide dynamics in landslide dominated drainage basins. *Journal of Geophysical Research: Earth Surface,* 114, F01007.

979 **Figure Captions**

980 Figure 1. Schematic architecture of the IC index, illustrating the relevant upslope
981 (Dup) and downslope (Ddn) components (after Borselli *et al.*, 2008). A = drainage
982 area; S = slope; d = flow path length; W = weighting factor (i.e., normalized surface
983 roughness in the index version modified by Cavalli *et al.* (2013)). The IC index, first
984 developed by Borselli et al. (2008), was later refined by Cavalli *et al.* (2013) for semi-
985 automated application to high-resolution Digital Terrain Models.

986 Figure 2. (a) Shaded relief map showing the location of the sampling sites (green
987 circles) along the study streams. (b) Shaded relief map of the Gadria and Strimm
988 source basins, and the Gadria fan. (c) Schematic view of the anthropogenic-induced
989 hydrologic and sedimentary pathways between the Gadria-Strimm and the Allitz-
990 Adige confluences. Note that, seasonally, water intercepted at the outlet of Strimm
991 Creek is conveyed directly to Allitz Creek bypassing the retention basin. In Allitz
992 Creek, water is intercepted again upstream of A1, and distributed for irrigation over
993 the Gadria fan.

994 Figure 3. Geological setting of the Gadria and Strimm basins showing the tectonic
995 contact (thick blue lines) between Mazia (blue) and Ötztal (orange) units. Thin blue
996 lines indicate strike-slip faults. DSGSD (Deep-Seated Gravitational Slope
997 Deformation) indicates the location of a sackung. Postglacial Quaternary valley fills
998 (white area) occupy the corridoor connecting the main Gadria valley floor with the
999 Gadria fan apex. See text for details.

1000 Figure 4. Long profiles of: (a) Gadria Creek and main tributaries; and (b) Strimm
1001 Creek and S3 tributary. Black circles locate sampling sites. Inset shows the plan view
1002 of the study streams.

1003 Figure 5. (a) Multi-temporal (1959-2012) mapping of sediment sources, including
1004 shallow landslide scars (red polygons), deposition lobes (green polygons), and
1005 patches of chronic surficial erosion (orange polygons). (b) Shallow debris-flow track
1006 near site S4. (c) Example of surficial erosion patcthes and shallow debris-flow lobes
1007 buffered by the floodplain in upper Strimm Creek, upstream of site S2. (d) Lakes
1008 nested in a relict hummocky moraine, downstream of site S1. Lakes form effective
1009 barriers to downstream sediment routing. Note in map that rock glaciers (violet

polygons) around site S1 are typically disconnected from shallow landslide activity. MHV = Main hanging valley; SHV = Secondary hanging valley.

Figure 6. Multi-temporal mapping of debris-flow disturbance in the Gadria and Strimm basins between 2008 and 2014. Red linework indicates debris-flow tracks; green circles indicate sampling locations. The debris flow mapped in 2011 (panel d) occurred on August 5, remobilized in-channel deposits, did not involve dissected tributary G1 in the DSGSD area, and deposited about 2000 m^3 of material at the retention basin (Table 1). Sand samples in 2014 were collected before the debris flow occurred on July 15, 2014 (panel f).

Figure 7. Time series of (a) ^{10}Be-nuclide concentrations, and (b) corresponding CWDRs, resulting from sand samples collected between October 2012 and July 2014, across (c) the nested arrangement of sampling sites. Single sampling sites are marked by unique color-coded symbols. Red arrows mark the occurrence of the debris flow in Gadria Creek. Error bars (i.e., blank error and analytical uncertainties) as described in Section 3.2, are used to discriminate significantly different concentrations (and relevant denudation rates) through time.

Figure 8. (a) Spatial distribution of IC* index in Gadria and Strimm basins; and (b) IC*index as a function of downstream distance. ^{10}Be concentrations (c and e) and corresponding CWDRs (d and f) as a function of the IC* index. Where IC*index = antilog (IC index). In Gadria and Strimm Creeks, the target used for IC* index calculations is the filter check dam at the outlet of the retention basin; in Allitz Creek, the target is the confluence with the Adige River. IC values at sites A1 and A2 are shown for illustrative purpose. In panel b, sampling site at colluvial tributary S3 is marked with an empty triangle, as opposed to sites along Strimm Creek (filled triangles). In panel c, d, e, and f, empty symbols refer to samples collected in October 2012, filled symbols represent 2013 and 2014 samples. Straight line indicates trend line fitted through Strimm and Gadria samples collected in October 2012.

Figure 9. Sampling sites (green circles) overlaid to maps of thresholded DoD (2005-2011) in Strimm (a) and Gadria (b) basins (after Cavalli *et al.,* 2017). In panel b, dashed green outline marks the extent of the sackung. Color scale ranges from red (erosion) to blue (deposition). To minimize noise, DoD analysis was performed within a buffer (thin black line) that includes areas displaying field and remotely-based

evidence of erosion and deposition. Based on this criterion, since erosion and deposition along the drainage network in proximity of site S1 was deemed below the DoD uncertainty threshold, most of the hanging valley floor in the Strimm was excluded from the analysis (see Cavalli *et al.,* 2017 for details).

Figure 10. (a) Frequency distribution of erosion depths (m) as obtained from thresholded DoD within sub-catchments draining to sampling sites S3 and G1 (2005-2011). DoD cell size is 2 meters. Helicopter views of sub-basins feeding sampling sites (b) G1 on July 23 2013; and (c) S3 on July 14 2010, after the occurrence of debris flows that deposited 20,000 m^3 in the retention basin (photos courtesy of Autonomous Province of Bolzano). Field views of (d) V-notched bedrock channel cutting through shattered lithologies at the upper end of sackung in G1; and (e) headmost portion of sub-basin S3 with sheet-wash erosion patches and shallow landsliding (red arrow points to the location of S3 sampling point, outside of photo view). Yellow circles indicate the locations of the sampling sites.

Figure 11. IC* index (a); basin-mean slope (b) and basin-mean normalized channel steepness index k_{sn} (c) as a function of basin-wide denudation rate. Empty symbols indicate samples collected in October 2012. Filled symbols indicate samples collected in 2013 and in July 2014. K_{sn} was obtained using TopoToolbox, following the sampling specifics described by Di Biase *et al.* (2010).

Figure 12. Sediment mixing model at sites A1 and A2 collected in: (a) October 2012; (b) July 2013; (c) October 2013; and (d) July 2014. Grey-shaded area indicates 10Be concentration (i.e., 1σ error around the 10Be concentration of the mixture) interpolated across the possible envelope of mixing ratios between the two source basins: Gadria (site G2) and Strimm (site S5) (x-axis). Vertical hatched area delimits the possible range of mixing based on the sediment volumes exported from each source basin (Table S2). When A1 (or A2) area overlaps with the grey shaded area outside of the hatched vertical area, insufficient mixing is inferred.

Figure 13. Schematic conceptual model describing the hydro-geomorphic functioning of the Gadria-Strimm confluence: (a) anthropogenic-altered hydro-geomorphic configuration that leads to the observed pronounced seasonal variability of [10Be]; and (b) hypothesized natural configuration in which seasonality may not be as significant.

Figure 14. (a) Schematic diagram illustrating the effects of contemporary perturbations induced on (apparent) ^{10}Be-derived denudation rates: at site G2 by the occurrence of a debris flow recruiting sediment beyond critical depth (blue line), and at site A1 by seasonal water diversion and the retention basin (green line). Red line indicates substantially stable rates at site S5; (b) Temporal variability and integration time scales of ^{10}Be-derived sediment yield at sites A1, G2 and S5 (this study) in the context of the paraglacial sedimentary wave of the Gadria fan (Brardinoni *et al.*, 2018); and (c) Area-slope plot of the longitudinal profiles of Gadria main stem and tributary G1. Note the distinctive unglaciated, debris-flow topographic signature in G1 tributary, with the main inflection point in the power-law relation at about 1 km^2. In panel (b), the length of each color-coded rectangle represents the relevant integration time scale (Table 3). For sites A1 and G2, end-member values within the Oct2012-July2014 time series are shown. Sediment yields associated with the Gadria fan building should be considered as minimum estimates, due to unknown variable trapping efficiency of the fan across various stages of development.

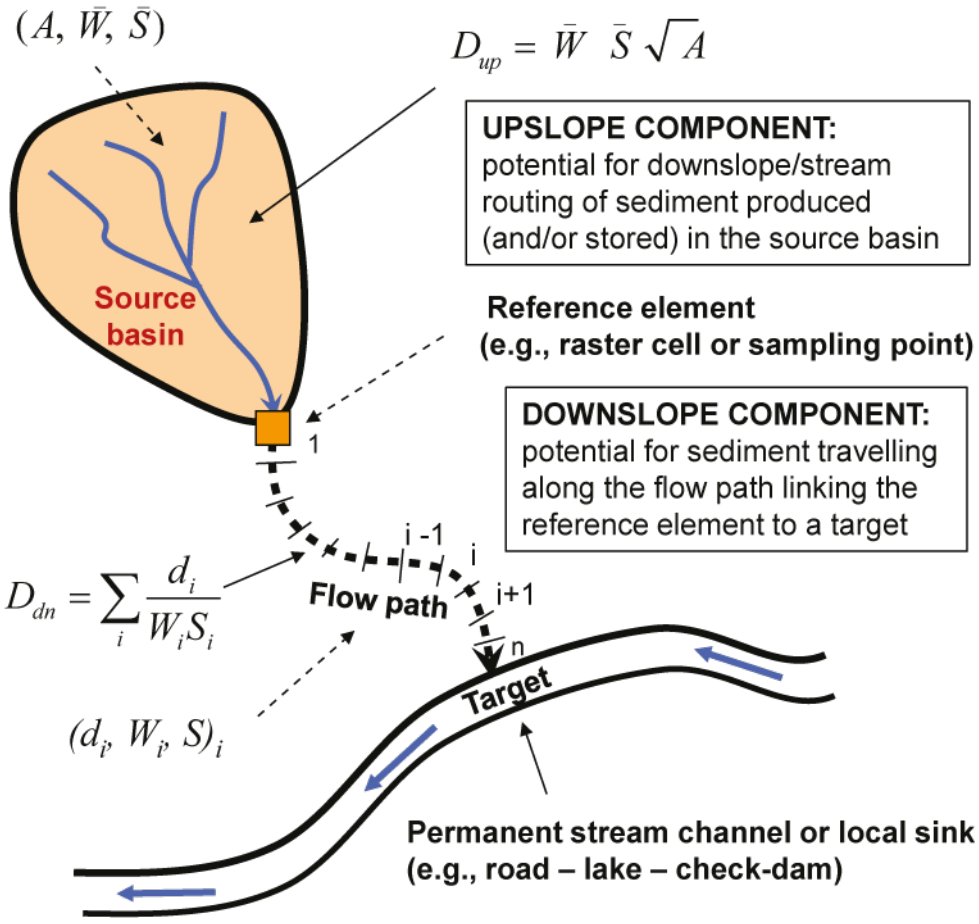
$(A, \bar{W}, \bar{S})$
$D_{up} = \bar{W}\ \bar{S}\ \sqrt{A}$
UPSLOPE COMPONENT:
potential for downslope/stream routing of sediment produced (and/or stored) in the source basin
Source basin
Reference element
(e.g., raster cell or sampling point)
DOWNSLOPE COMPONENT:
potential for sediment travelling along the flow path linking the reference element to a target
1
i -1
i
i+1
n
$D_{dn} = \sum_i \frac{d_i}{W_i S_i}$
Flow path
$(d_i, W_i, S)_i$
Target
Permanent stream channel or local sink
(e.g., road – lake – check-dam)

Figure 1.

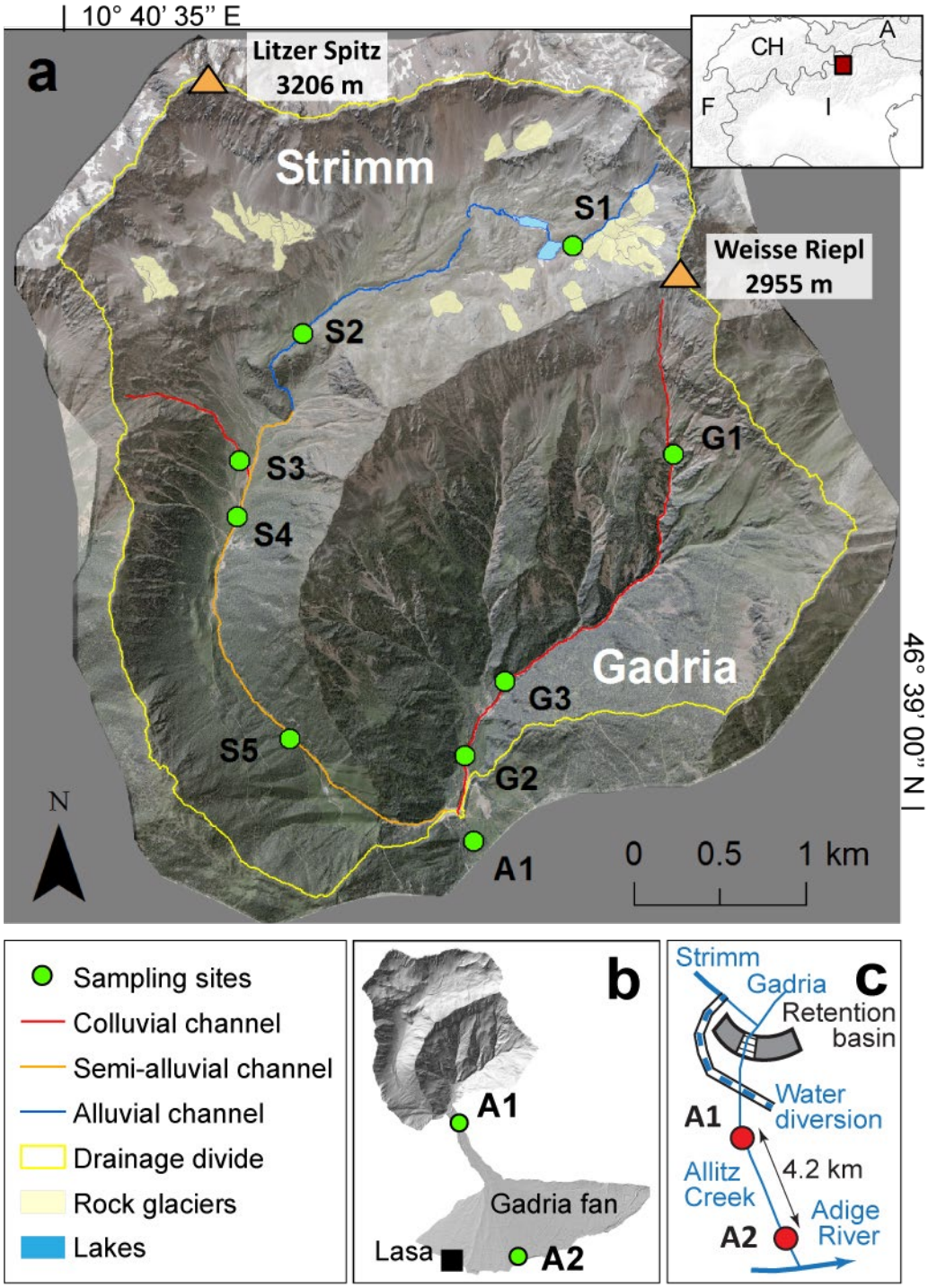
10° 40' 35" E
a
Litzer Spitz
3206 m
Strimm
S1
Weisse Riepl
2955 m
S2
G1
S3
S4
Gadria
G3
S5
G2
A1
N
0 0.5 1 km
46° 39' 00" N
CH
A
F
I
Sampling sites
Colluvial channel
Semi-alluvial channel
Alluvial channel
Drainage divide
Rock glaciers
Lakes
b
A1
Gadria fan
Lasa
A2
Strimm
Gadria
c
Retention basin
Water diversion
A1
Allitz Creek
4.2 km
Adige River
A2

Figure 2.

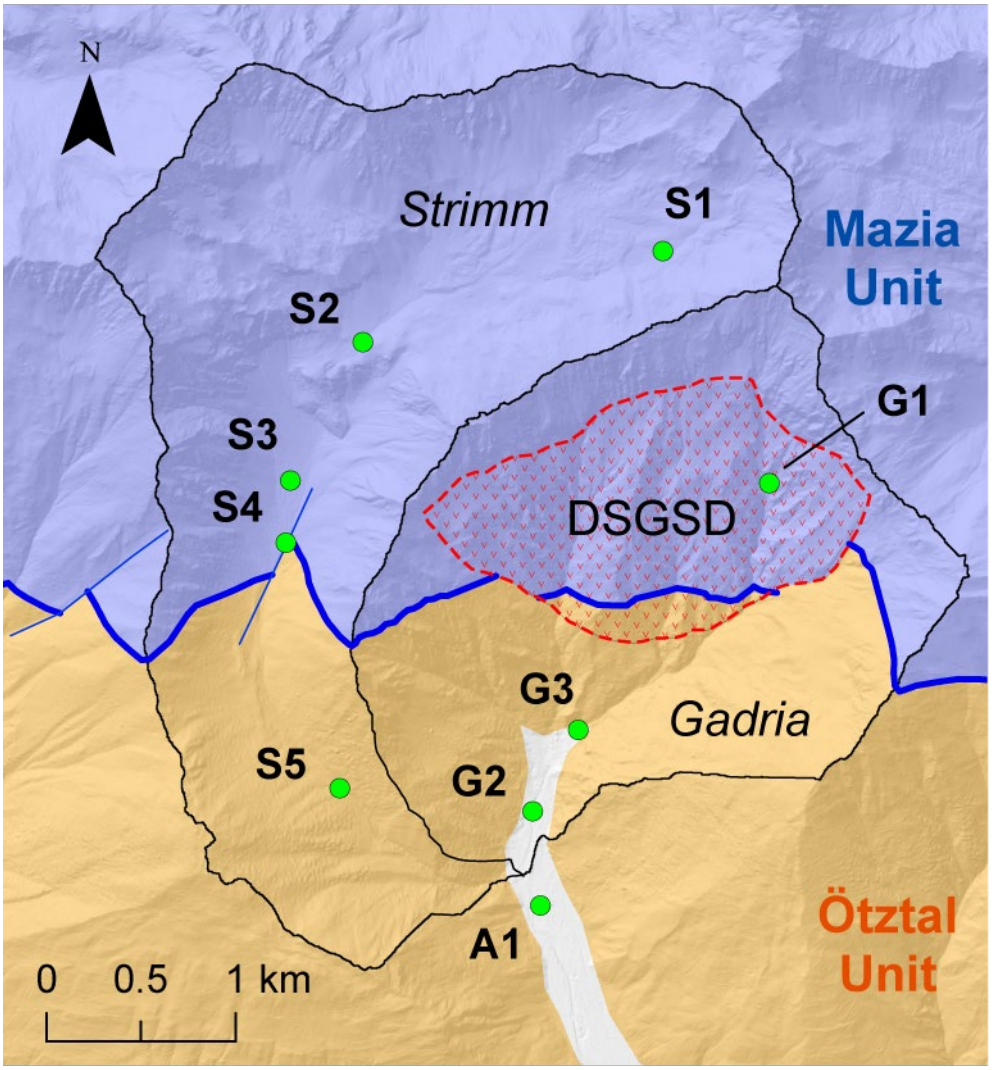
N
Strimm
S1
Mazia
Unit
S2
G1
S3
S4
DSGSD
G3
Gadria
S5
G2
A1
Ötztal
Unit
0
0.5
1 km

Figure 3.

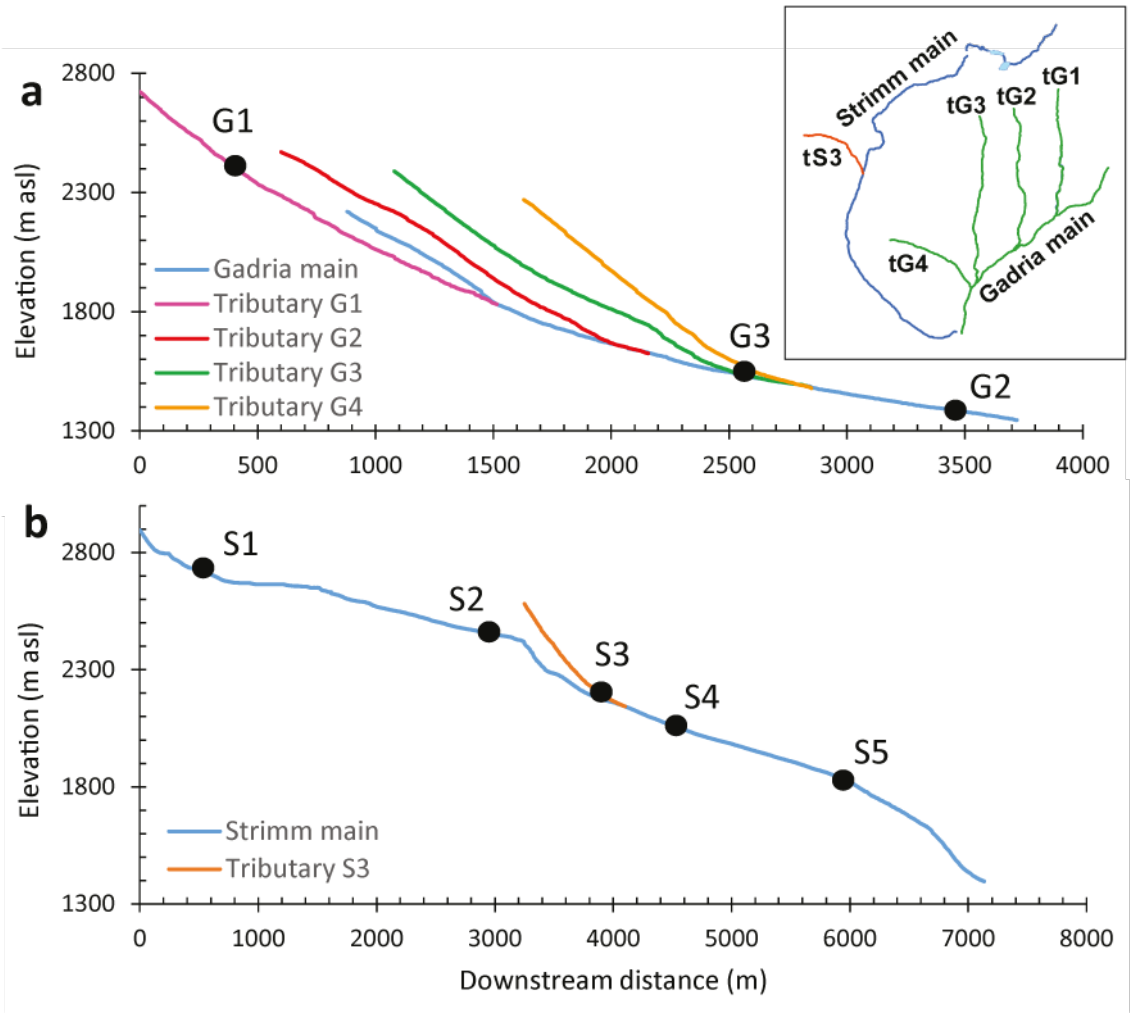
a
Elevation (m asl)
2800
2300
1800
1300
0
500
1000
1500
2000
2500
3000
3500
4000
G1
G2
G3
Gadria main
Tributary G1
Tributary G2
Tributary G3
Tributary G4
Strimm main
tG1
tG2
tG3
tS3
tG4
Gadria main
b
Elevation (m asl)
2800
2300
1800
1300
0
1000
2000
3000
4000
5000
6000
7000
8000
S1
S2
S3
S4
S5
Strimm main
Tributary S3
Downstream distance (m)

Figure 4.

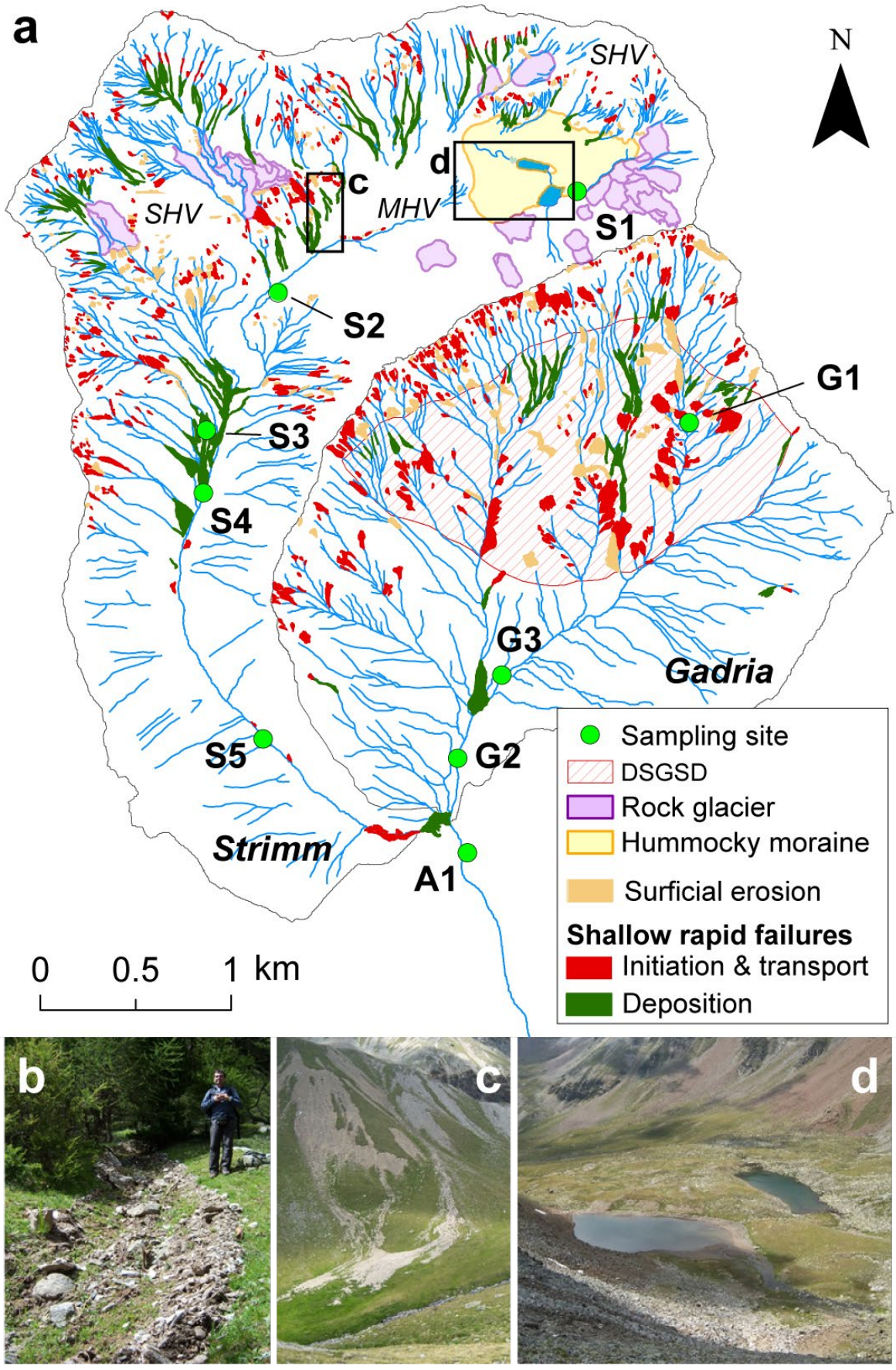
a
N
SHV
SHV
MHV
c
d
S1
S2
S3
S4
S5
G1
G2
G3
A1
Gadria
Strimm
0 0.5 1 km
Sampling site
DSGSD
Rock glacier
Hummocky moraine
Surficial erosion
Shallow rapid failures
Initiation & transport
Deposition
b
c
d

Figure 5.

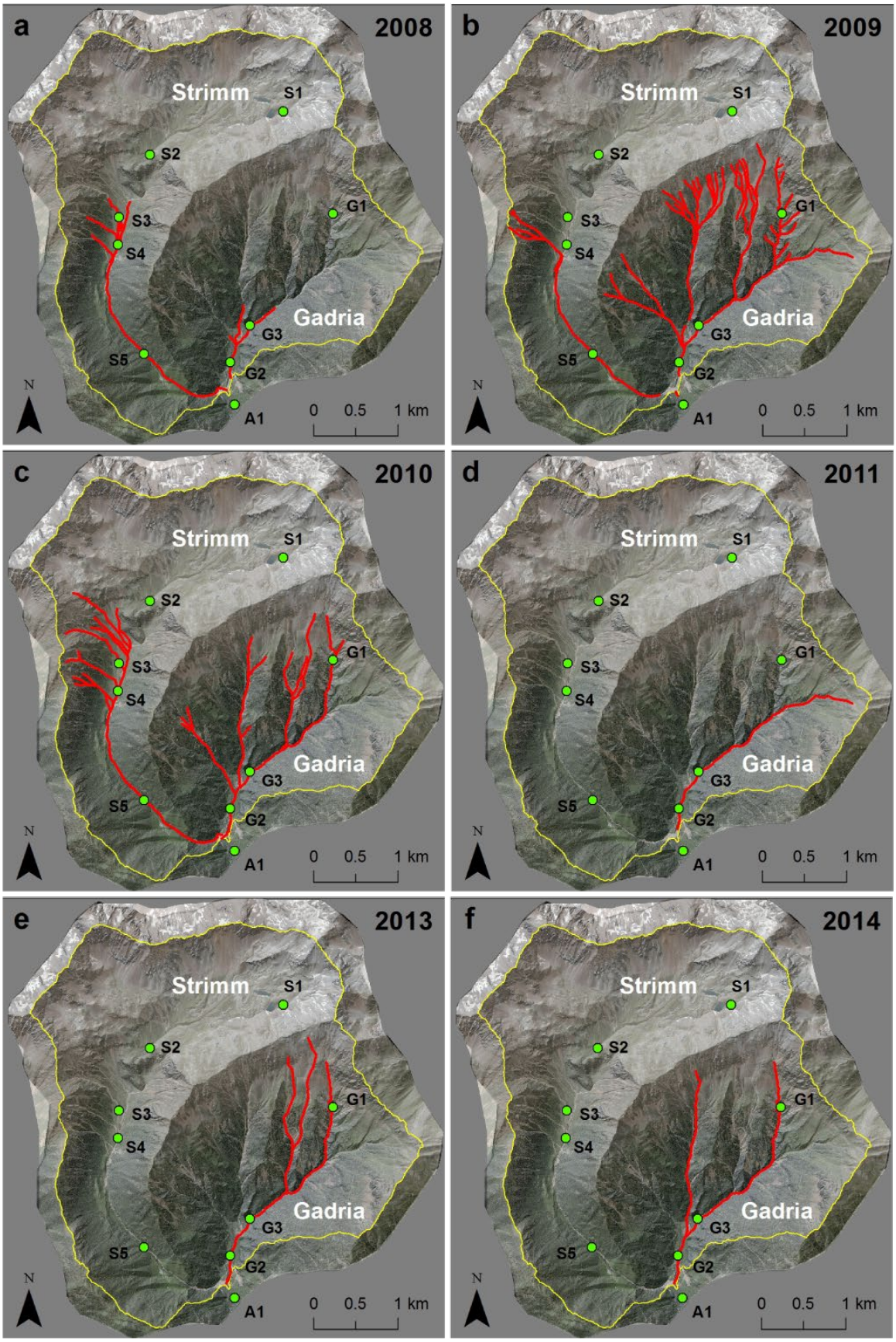
a
2008
Strimm
S1
S2
S3
S4
S5
G1
G2
G3
Gadria
A1
N
0 0.5 1 km
b
2009
c
2010
d
2011
e
2013
f
2014

Figure 6.

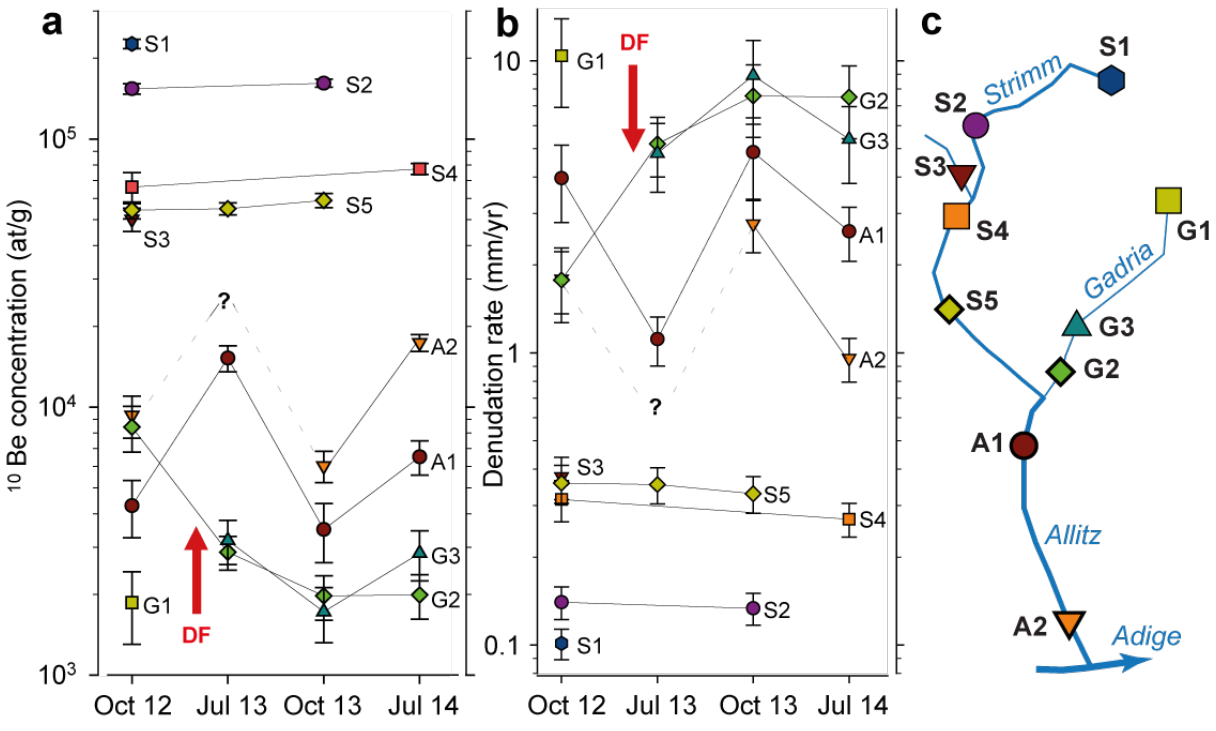
a
b
c
S1
S2
S3
S4
S5
A1
A2
G1
G2
G3
DF
?
^{10}Be concentration (at/g)
Denudation rate (mm/yr)
Oct 12
Jul 13
Oct 13
Jul 14
Strimm
Gadria
Allitz
Adige

Figure 7.

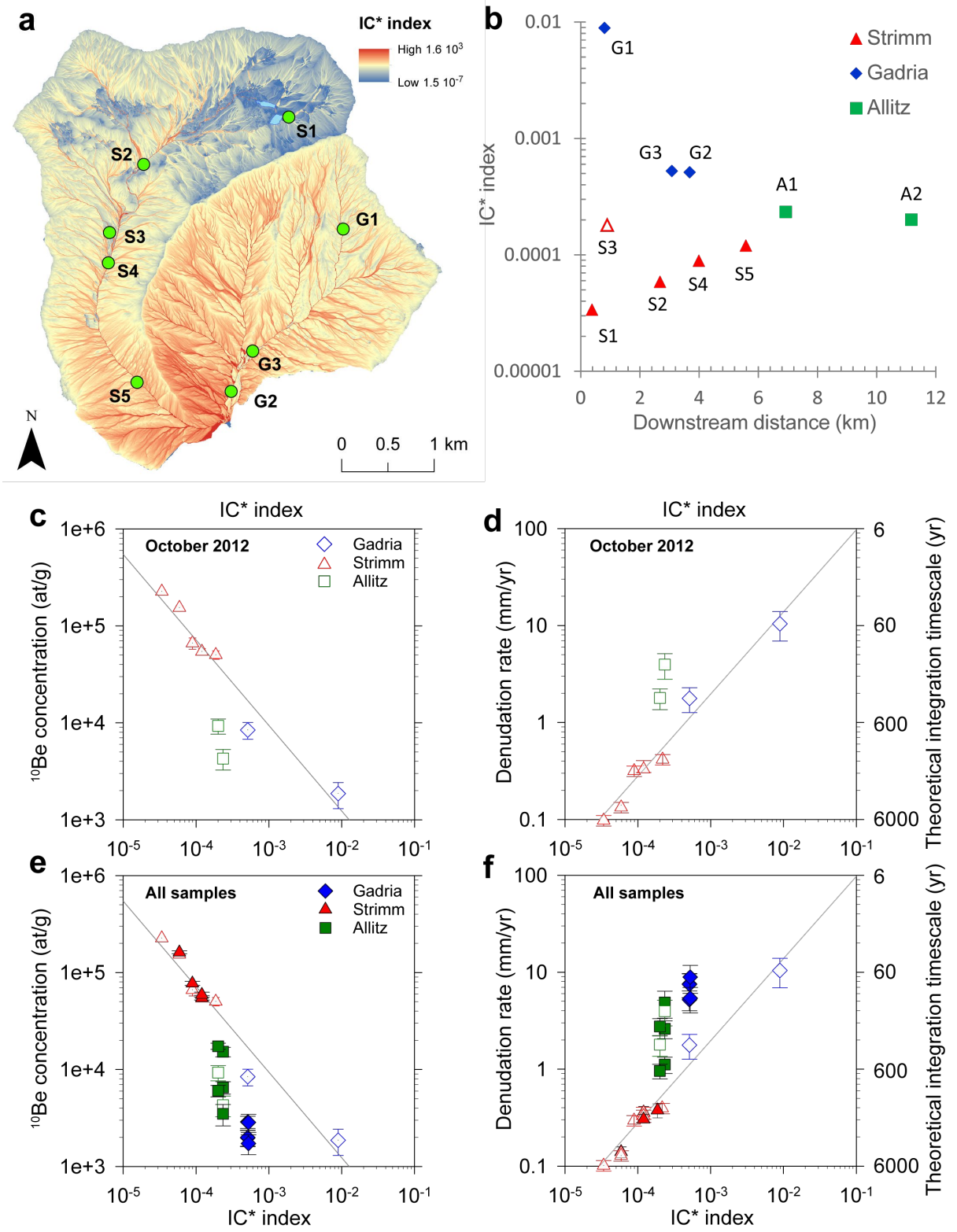
a
IC* index
High 1.6 10^3
Low 1.5 10^-7
S1
S2
S3
S4
S5
G1
G2
G3
N
0 0.5 1 km
b
IC* index
Downstream distance (km)
Strimm
Gadria
Allitz
G1
G3
G2
A1
A2
S3
S5
S4
S2
S1
c
IC* index
October 2012
Gadria
Strimm
Allitz
10Be concentration (at/g)
d
IC* index
October 2012
Denudation rate (mm/yr)
Theoretical integration timescale (yr)
e
All samples
Gadria
Strimm
Allitz
10Be concentration (at/g)
IC* index
f
All samples
Denudation rate (mm/yr)
Theoretical integration timescale (yr)
IC* index

Figure 8.

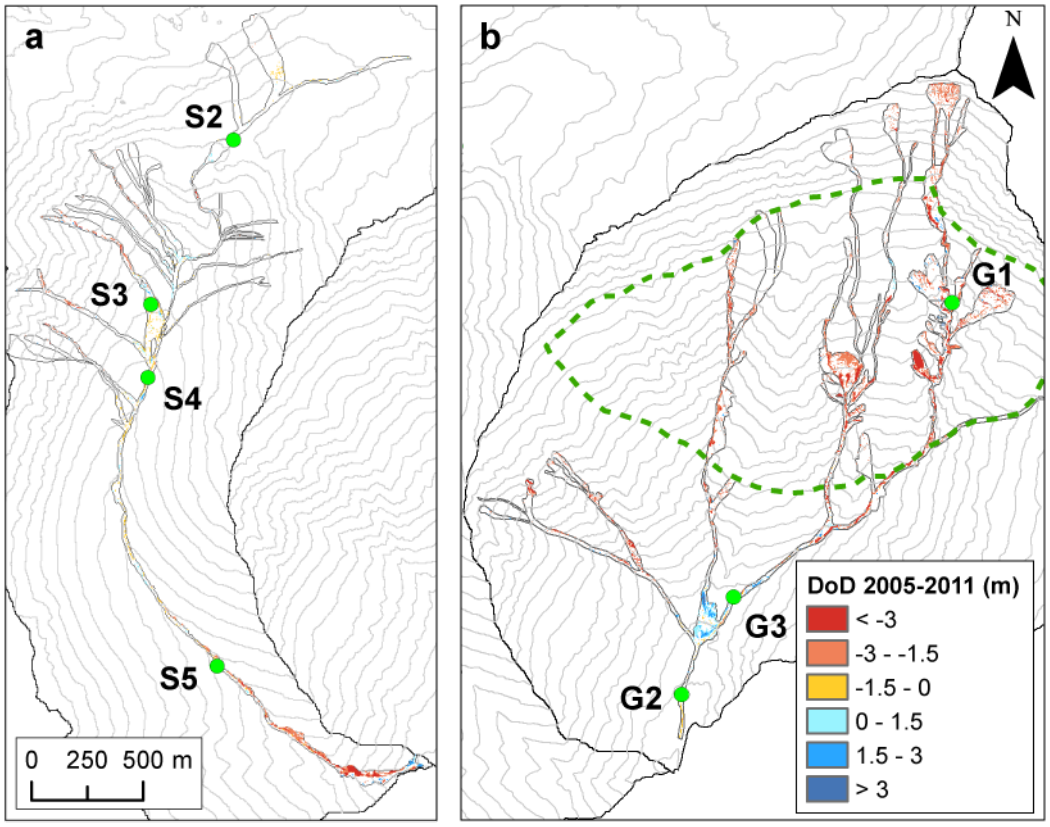
a
S2
S3
S4
S5
0 250 500 m
b
N
G1
G3
G2
DoD 2005-2011 (m)
< -3
-3 - -1.5
-1.5 - 0
0 - 1.5
1.5 - 3
> 3

Figure 9.

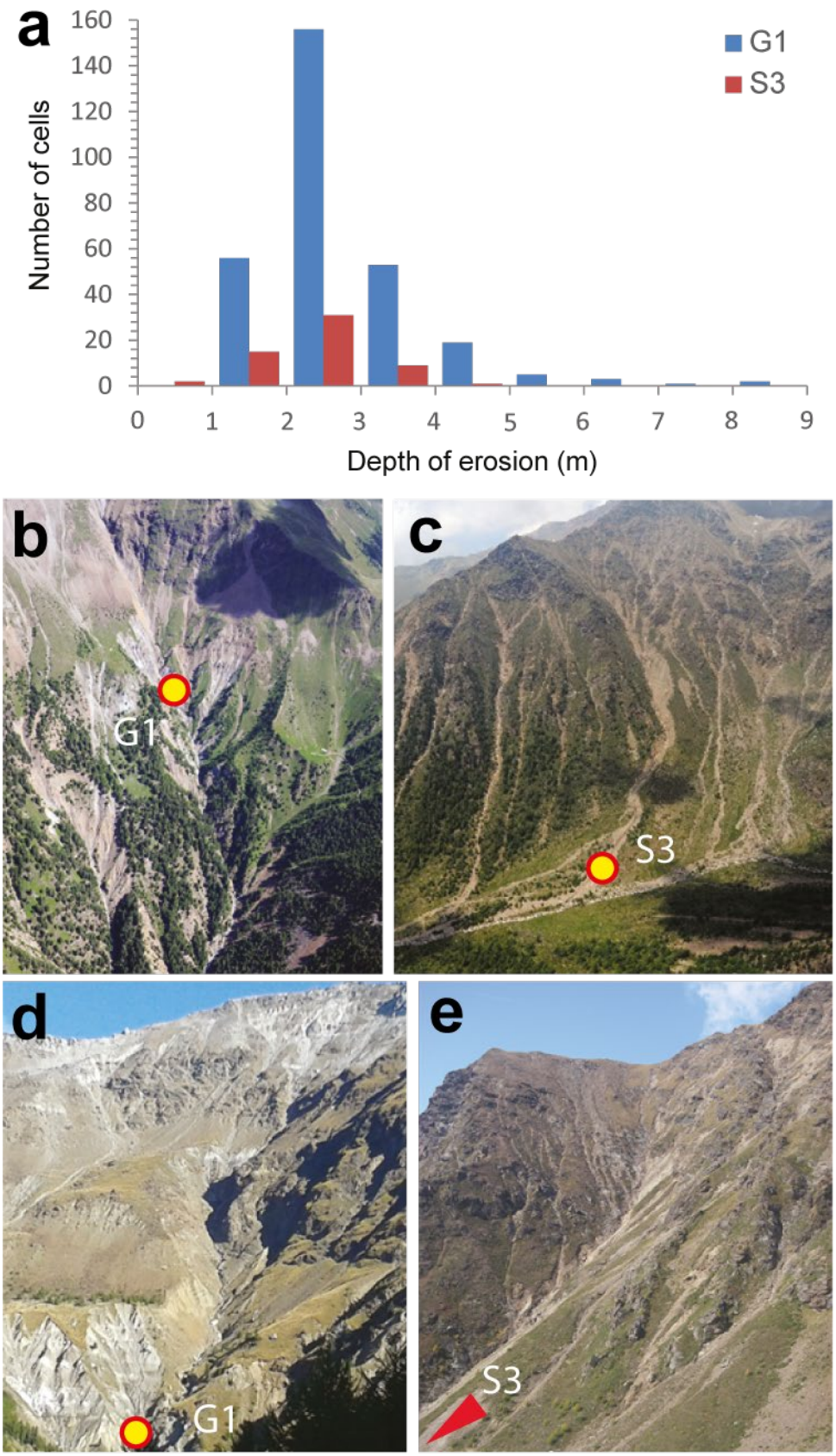
a
Number of cells
160
140
120
100
80
60
40
20
0
0 1 2 3 4 5 6 7 8 9
Depth of erosion (m)
G1
S3
b
G1
c
S3
d
G1
e
S3

Figure 10.

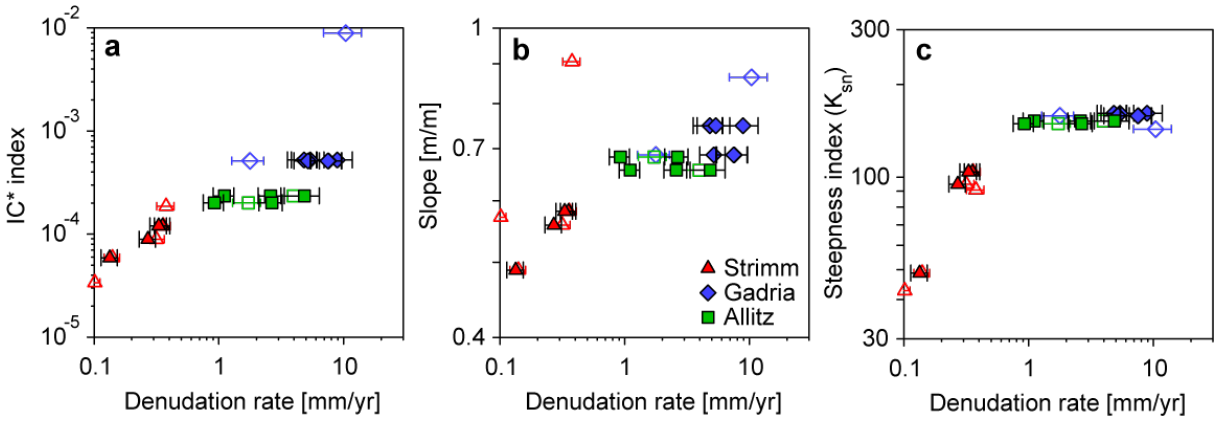
a
IC* index
Denudation rate [mm/yr]
b
Slope [m/m]
Denudation rate [mm/yr]
Strimm
Gadria
Allitz
c
Steepness index (K_{sn})
Denudation rate [mm/yr]

Figure 11.

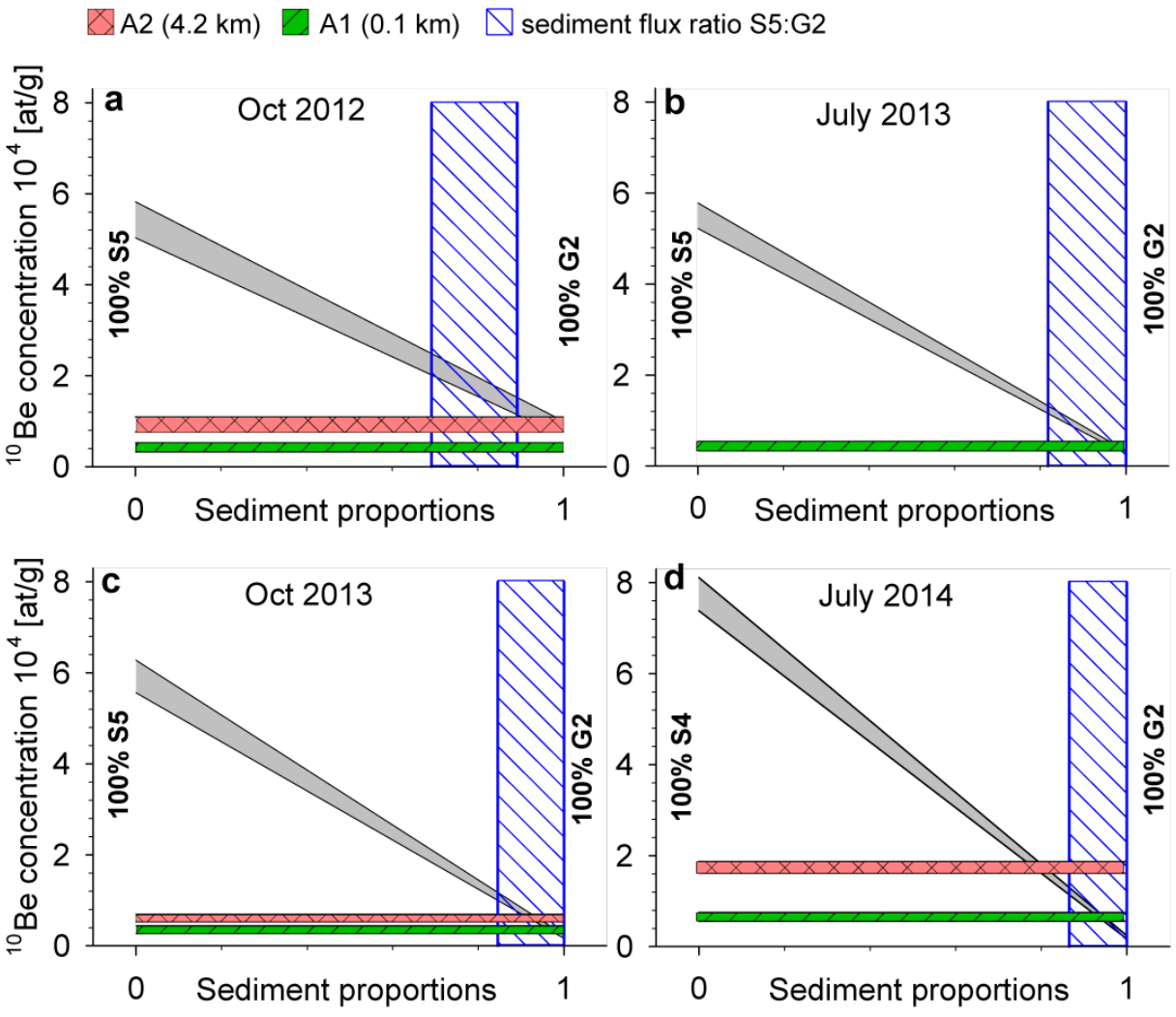
A2 (4.2 km)
A1 (0.1 km)
sediment flux ratio S5:G2
a
Oct 2012
b
July 2013
c
Oct 2013
d
July 2014
100% S5
100% S4
100% G2
^{10}Be concentration 10^4 [at/g]
Sediment proportions
0
1
2
4
6
8

Figure 12.

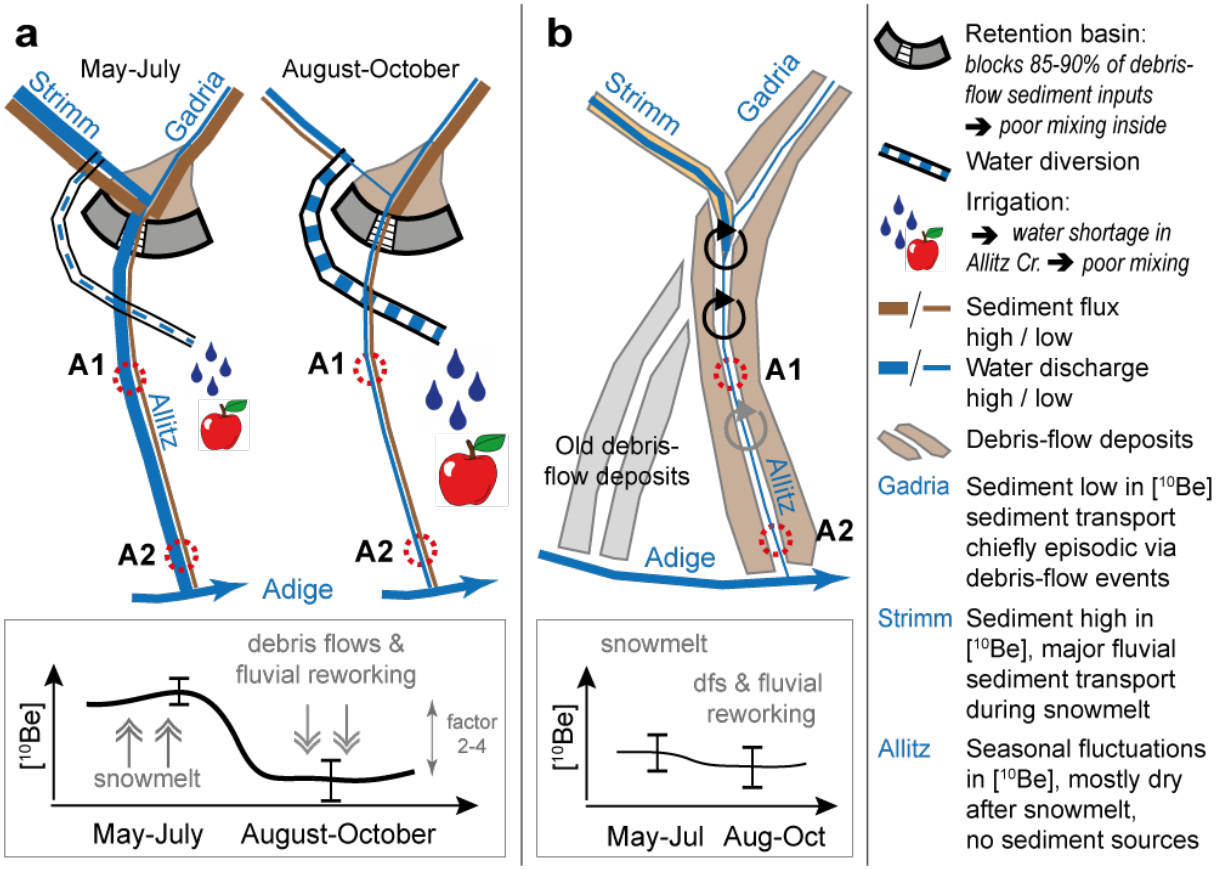
a
May-July
August-October
Strimm
Gadria
A1
A2
Allitz
Adige
b
Old debris-flow deposits
debris flows & fluvial reworking
snowmelt
factor 2-4
[10Be]
May-July
August-October
dfs & fluvial reworking
May-Jul
Aug-Oct
Retention basin: blocks 85-90% of debris-flow sediment inputs → poor mixing inside
Water diversion
Irrigation: → water shortage in Allitz Cr. → poor mixing
Sediment flux high / low
Water discharge high / low
Debris-flow deposits
Gadria Sediment low in [10Be] sediment transport chiefly episodic via debris-flow events
Strimm Sediment high in [10Be], major fluvial sediment transport during snowmelt
Allitz Seasonal fluctuations in [10Be], mostly dry after snowmelt, no sediment sources

Figure 13.

1224

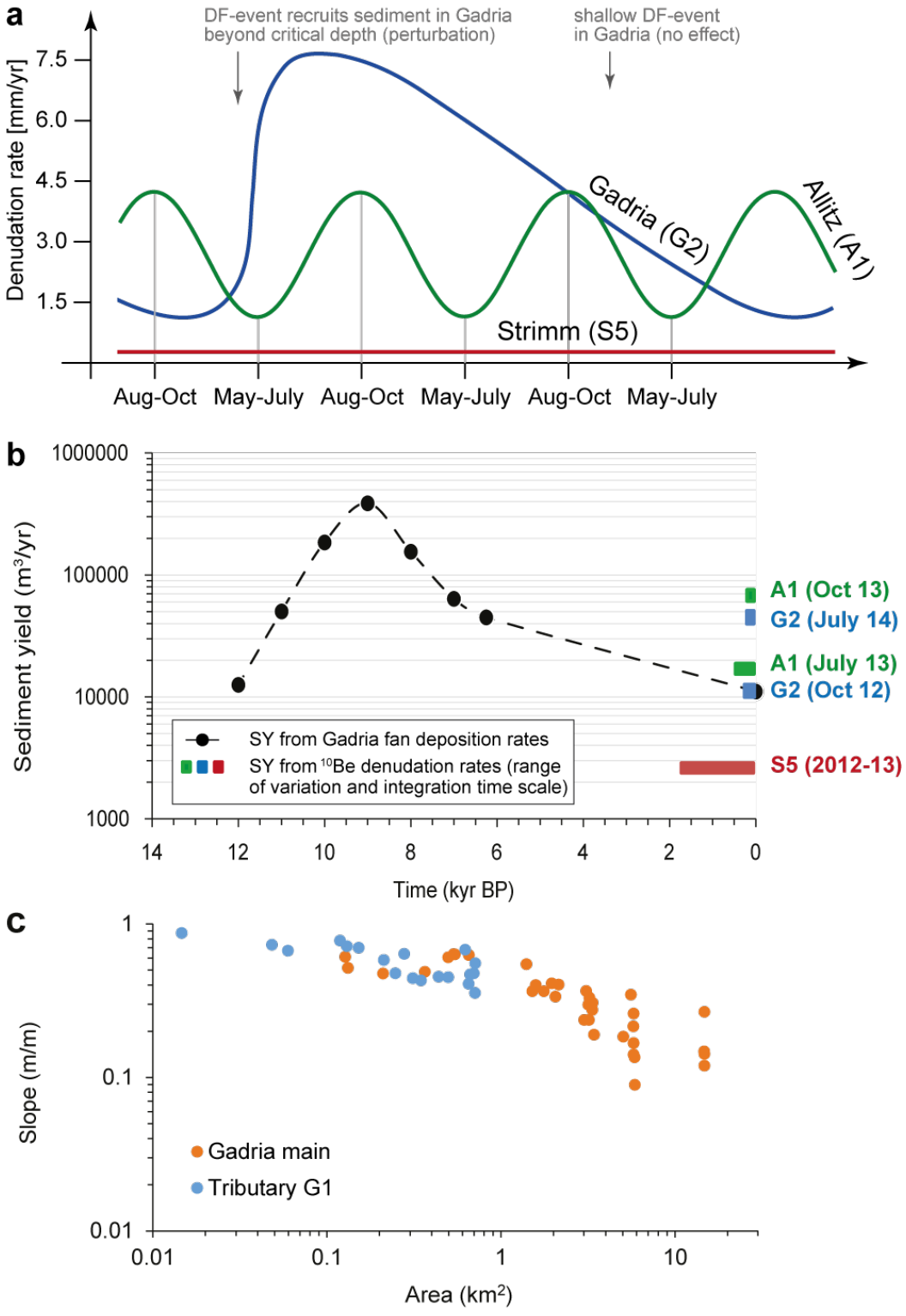

1225

1226 Figure 14.

1227

1228

1229 Table 1. Debris-flow occurrence in the Gadria basin and deposited volumes of
1230 sediment at the retention basin (2008-2014).

Date (dd/mm/yy)	Deposited volume at the retention basin (m^3)
06/08/2008	27,100
24/07/2009	35,000
12/07/2010	20,000
05/08/2011	2,000
18/07/2013	8,100
15/07/2014	10,400

1231
1232
1233 Table 2. Sand samples collected between 2012 and 2014. All samples were sieved
1234 to a grain-size range of 250-1000 µm.

Sampling Site	Basin area (km^2)	Elevation (m asl)	Sample ID	Sampling date (MM/YY)	Carrier weight (mg)	Sample weight (g)	^{10}Be (at/g/yr) x 10^3	1σ error (at/g/yr) x 10^3	CWDR (mm/yr)	Uncertainty (mm/yr)
G1	0.31	2174	G1 1012	10/12	0.243	49.2	1.865	0.562	10.41	3.49
G2	5.78	1416	G2 1012	10/12	0.251	44.5	8.421	1.642	1.78	0.51
			G2 0713	07/13	0.199	55.6	2.877	0.412	5.20	1.20
			G2 1013	10/13	0.201	54.7	1.975	0.373	7.57	2.11
			G2 0714	07/14	0.197	41.2	1.992	0.374	7.51	2.10
G3	3.36	1510	G3 0713	07/13	0.204	53.2	3.181	0.595	4.82	1.28
			G3 1013	10/13	0.202	40.8	1.723	0.401	8.90	2.84
			G3 0714	07/14	0.191	42.5	2.847	0.601	5.39	1.58
S1	0.41	2671	S1 1012	10/12	0.249	41.5	226.301	9.103	0.10	0.01
S2	3.16	2442	S2 1012	10/12	0.253	41.3	153.887	6.709	0.14	0.02
			S2 1013	10/13	0.257	28.7	161.458	5.654	0.13	0.02
S3	0.19	2155	S3 1012	10/12	0.253	30.3	50.191	4.974	0.38	0.06
S4	5.86	2080	S4 1012	10/12	0.257	35.3	66.201	8.771	0.31	0.05
			S4 0714	07/14	0.256	33.2	77.347	3.642	0.27	0.04
S5	7.61	1828	S5 0713	07/13	0.250	34.1	54.913	2.797	0.35	0.05
			S5 1012	10/12	0.230	44.3	54.276	3.961	0.36	0.05
			S5 1013	10/13	0.250	21.7	59.013	3.573	0.33	0.05
A1	14.7	1383	A1 1012	10/12	0.241	37.7	4.284	1.033	3.96	1.17
			A1 0713	07/13	0.370	37.2	15.231	1.703	1.11	0.21
			A1 1013	10/13	0.194	41.2	3.493	0.869	4.86	1.51
			A1 0714	07/14	0.189	53.2	6.521	0.952	2.60	0.54
A2	15.2	827	A2 1012	10/12	0.250	40.0	9.311	1.661	1.72	0.43
			A2 1013	10/13	0.202	52.3	6.032	0.808	2.66	0.56
			A2 0714	07/14	0.201	59.7	17.387	1.273	0.92	0.17

1235
1236
1237
1238
1239
1240
1241

1242 Table 3. Sand samples collected between 2012 and 2014, and time scales over
1243 which denudation rates and corresponding sediment yields are averaged.

Sampling Site	Sample ID	Sampling time (MM/YY)	^{10}Be (at/g/yr) x 10^3	CWDR (mm/yr)	Sediment yield (m^3/yr)	Averaging time scale (yr)
G1	G1 1012	10/12	1.865	10.41	3242	60
G2	G2 1012	10/12	8.421	1.78	10287	330
	G2 0713	07/13	2.877	5.20	30043	110
	G2 1013	10/13	1.975	7.57	43766	80
	G2 0714	07/14	1.992	7.51	43385	80
G3	G3 0713	07/13	3.181	4.82	16181	120
	G3 1013	10/13	1.723	8.90	29880	70
	G3 0714	07/14	2.847	5.39	18080	110
S1	S1 1012	10/12	226.301	0.10	41	5850
S2	S2 1012	10/12	153.887	0.14	442	4230
	S2 1013	10/13	161.458	0.13	421	4440
S3	S3 1012	10/12	50.191	0.38	72	1570
S4	S4 1012	10/12	66.201	0.31	1844	1880
	S4 0714	07/14	77.347	0.27	1578	2200
S5	S5 0713	07/13	54.913	0.35	2729	1650
	S5 1012	10/12	54.276	0.36	2698	1670
	S5 1013	10/13	59.013	0.33	2510	1800
A1	A1 1012	10/12	4.284	3.96	58292	150
	A1 0713	07/13	15.231	1.11	16339	530
	A1 1013	10/13	3.493	4.86	71540	120
	A1 0714	07/14	6.521	2.60	38272	230
A2	A2 1012	10/12	9.311	1.72	26192	340
	A2 1013	10/13	6.032	2.66	40507	220
	A2 0714	07/14	17.387	0.92	14010	640

1244